

Chapter 10

The Superconducting Inflector Magnet

In this chapter we first introduce the E821 inflector magnet, which is our baseline starting option. We then describe the shortcomings of this magnet, as well as the characteristics and the benefits that an improved inflector would have. During the period between the CD1 Review and the present, an Inflector Task Force (ITF) [1] has been set up to develop a design for a new inflector. Two options are being explored: A direct wind magnet using the technique developed at Brookhaven Lab by Brett Parker, and a double cosine theta magnet following the E821 design, but with open ends and a wider beam channel.

At present the new inflector is outside of the scope of the project budget cap. Because of the real benefits to the experiment, the new inflector is being studied as an ‘optional scope contingency’, to be brought into the baseline if we prove contingency is available. We will continue the design work, so that if/when adequate contingency becomes available, we can move forward with the production.

10.1 Introduction to Inflection Challenges

The typical storage ring is composed of lumped beamline elements such as dipoles, quadrupoles, sextapoles, etc., which leaves space for injection, extraction, and other beam manipulation devices. For the measurement of a_μ , the requirement of ± 1 ppm uniformity on the magnetic field, which in E989 must be known to $\leq \pm 70$ ppb, prohibits this usual design. Instead, as described in Chapter 9 the $(g - 2)$ storage ring is designed as a monolithic magnet with no end effects. The “C”-magnet construction shown in Fig 9.1 presents several obstacles to transporting a beam into the storage ring: There must be holes through the back-leg of the magnet and through the outer coil cryostat and mandrel for the beam to enter the experiment. These holes must come through at an angle, rather than radially, which complicates the design, especially of the outer-coil cryostat.

A plan view of the beam path entering the storage ring is given in Fig. 10.1. Since the beam enters through the fringe field of the magnet, and then into the main 1.5 T field, it will be strongly deflected unless some magnetic device is present that cancels this field. This device is called the inflector magnet. In reality, there is a fringe field that grows

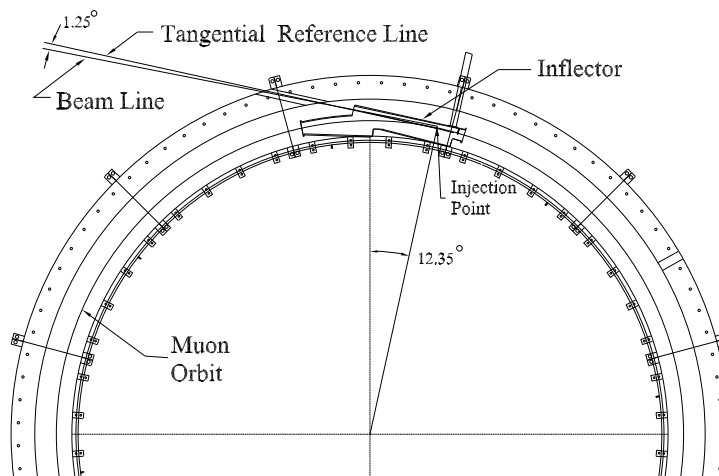


Figure 10.1: Plan view of the beam entering the storage ring.

approximately linearly as the beam moves radially inward from the hole in the outer cryostat to the location of the inflector entrance. This is sketched in Fig. 10.2.

The injection beam line is set to a 1.25° angle from the tangential reference line (Fig. 10.1). The inflector is aligned along this reference line and its downstream end is positioned at the injection point, which is tangent to the ring. The point where the reference line is tangent to the storage ring circumference is offset 77 mm radially outward from the muon central orbit. The main magnet fringe field, upstream of the inflector, bends the incoming beam by about 1.25° , so that the beam enters the inflector nearly parallel to the inflector axis.

The requirements on the inflector magnet are very restrictive:

1. To a good approximation it should null the storage ring field such that the muons are not deflected by the main 1.5 T field.
2. It should be a static device *to prevent time-varying magnetic fields correlated with injection*, which could affect $\int \vec{B} \cdot d\vec{\ell}$ seen by the stored muons and produce an “early to late” systematic effect.
3. It cannot “leak” magnetic flux into the precision shimmed storage-ring field that affects $\int \vec{B} \cdot d\vec{\ell}$ at the sub-ppm level.
4. It cannot contain any ferromagnetic material, which would distort the uniform magnetic field.
5. The inflector should have a “reasonable” aperture to match the beamline to the ring acceptance.
6. The inflector angle in the cryostat should be variable over the full range permitted by the constraints of the space available.

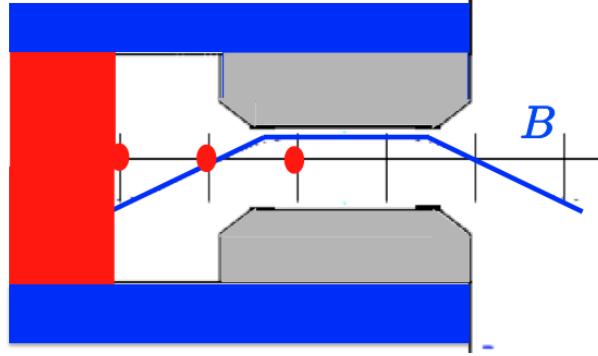


Figure 10.2: The fringe field of the main magnet over the radial range traversed by the beam. The left-hand red dot is where the beam exits hole in the outer coil. The center dot is where the beam enters the inflector. The right-hand dot is where the beam exits the inflector. The field inside of the inflector is not constant until part way down.

10.2 The E821 Inflector Design and Operation

Three possible solutions were considered in E821: A pulsed inflector, a superconducting flux exclusion tube, and a modified double $\cos\theta$ magnet. The pulsed inflector proved to be technically impossible at the repetition rate necessary at BNL. Furthermore it violates item 2 above. Naively one could imagine that a superconducting flux exclusion tube would work for this application. However, an examination of Fig. 10.3 shows that in the vicinity of the tube, the magnetic field is perturbed on the order of 10%, or 100,000 ppm [2], an unacceptable level. Attempts to figure out how to mitigate this problem were unsuccessful. This is because the large eddy currents needed to shield the 1.45 T field are large enough to affect the uniformity of the field seen by the muons contained in the red semicircle. However, this principle will re-appear in the discussion of how to shield the 200 G (20 mT) residual magnetic field from the truncated double $\cos\theta$ design employed in the E821 inflector. The properties of the E821 Inflector are summarized in Table 10.1

Table 10.1: Properties of the E821 Inflector.

Overall dimension	110(W) × 150(W) × 2025(L) mm ³
Magnetic length	1700 mm
Beam aperture	18 mm (W) × 56 mm (H)
Design current	2850 A (with 1.45 T main field)
Number of turns	88
Channel field	1.5 T (without main field)
Peak field	3.5 T (at design current, with main dipole field)
Inductance	2.0 mH
Resistance	1.4 Ω (at 300 K)
Cold mass	60 kg
Stored energy	9 kJ (at design current)

Table 10.2: Properties of the inflector superconductor.

Configuration (NbTi:Cu:Al)	1:0.9:3.7
Stabilizer	Al (99.997% RRR = 750)
Process	Co-extrusion
NbTi/Cu composite	Diameter 1.6 mm monolith
NbTi filament	Diameter 0.02 mm
Number of filaments	3050
Twist pitch	31 mm
Conductor dimension	2 × 3 mm ²
Insulated conductor dimension	2.3 × 3.3 mm ²

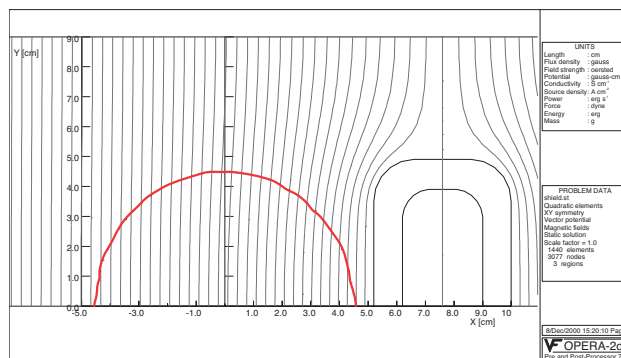


Figure 10.3: The calculated magnetic field outside of a superconducting flux exclusion tube placed in a 1.45 T magnetic field. The red circle is the muon beam storage region. (From Ref. [2])

10.2.1 Magnetic Design of the E821 Inflector

Only the double $\cos \theta$ design[4] satisfied the three criteria listed above. The double $\cos \theta$ design has two concentric $\cos \theta$ magnets with equal and opposite currents, which outside has negligible field from Ampère's law. A double $\cos \theta$ design provides a 1.5 T field close to the storage region, and traps its own fringe field, with a small residual fringe field remaining. However, what is needed for the $(g - 2)$ beam channel is a septum magnet. This is achieved by truncating the two $\cos \theta$ distributions along a line of constant vector potential A [4]. The truncation method is shown in Fig. 10.4, taken from Ref. [4], which should be consulted for additional details.

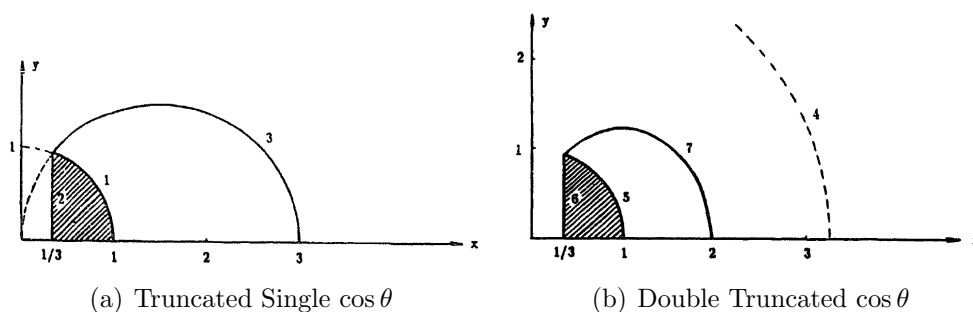


Figure 10.4: (a) The principle of the truncated single $\cos \theta$ magnet. (b) The principle of the truncated double $\cos \theta$ magnet.

Aluminum-stabilized superconductor was chosen for the BNL $(g - 2)$ inflector: (a) to minimize the interactions of the incoming pion/muon beam at both upstream and downstream ends of the coil with no open apertures for the beam, and (b) to make the coils and cryostat design compact, so that the conductive cooling (without liquid helium containers surrounding the coils) can be achieved effectively. An existing Al-stabilized superconductor was supplied by Japan KEK (fabricated by Furukawa Co.). This conductor was developed

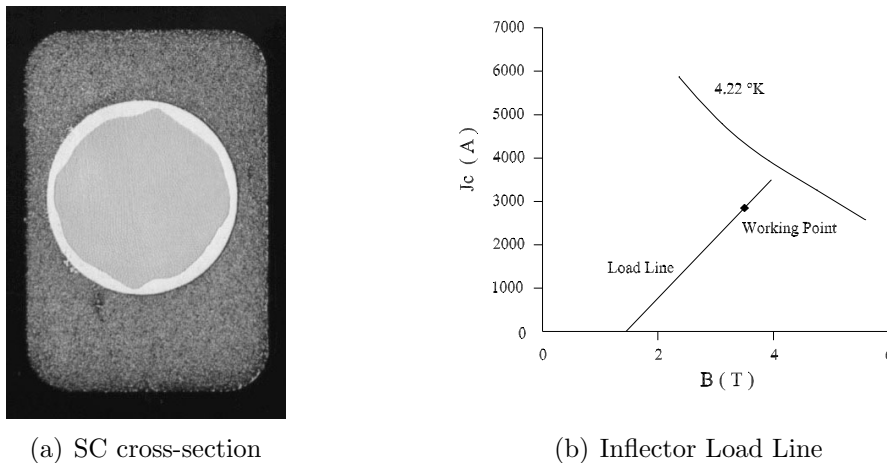


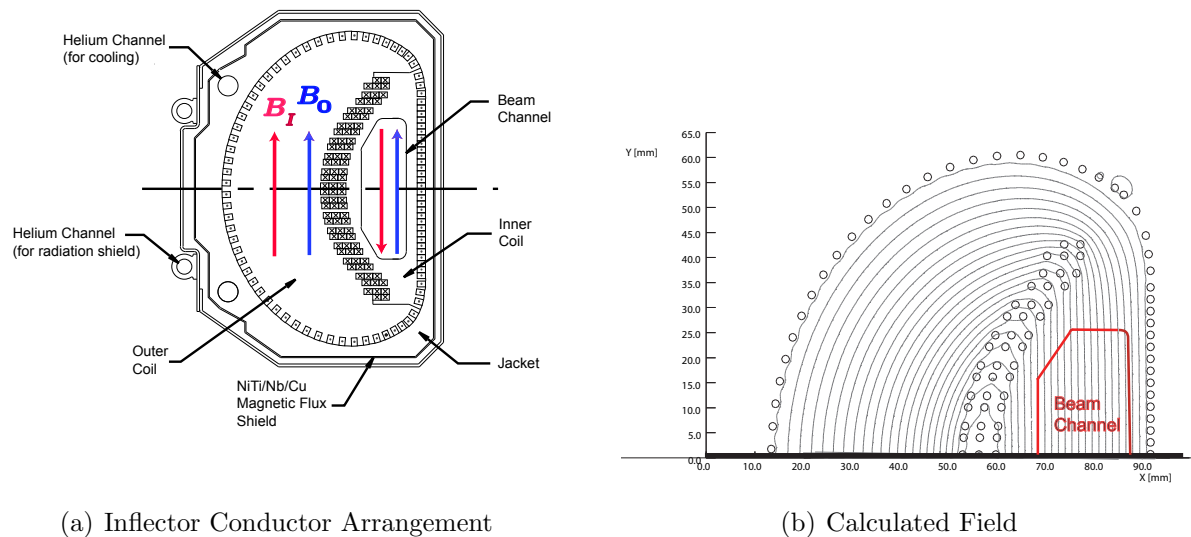
Figure 10.5: (a) The inflector superconductor cross-section. (b) Superconductor characteristics and the inflector load line in the environment of 1.45 T magnetic field.

for ASTROMAG (Particle Astrophysics Magnet Facility) [5, 6]. Fig. 10.5 shows the cross-section of this conductor. The basic parameters are listed in Table 10.2. From computer calculations, which include the self-field effect [7], show that the peak field seen by the inflector conductor filaments reaches 3.5 T. This is due to the superposition of the return flux and the main field. Short sample tests showed that the critical current of this superconductor is about 3890 A at 4.6 K and 3.5 T. In the $(g - 2)$ storage ring, the inflector sees 1.45 T field (from the main magnet) even at zero operating current. From the conductor characteristics, the inflector operates at around 73% of the full load (at 4.6 K). The short sample test data and the inflector load line (in the storage ring field environment) are shown in Fig. 10.5(b).

The result is a magnet with conductors arranged as shown in Fig. 10.6(a). The conductors are connected in series, with an equal number with current into and out of the page. In Fig. 10.6(a) the current is flowing out of the page in the backward “D” shaped pattern of conductors, and into the page in the “C” shaped arrangement of conductors. The field from the inflector magnet is vertical up in the beam channel and downward in the return area, as shown in Fig 10.6(a). With the main storage ring field vertical, there is no field in the beam channel and $\simeq 3$ T field in the return area. With this design and the ASTROMAG conductor, it is difficult to enlarge the beam channel very much because moving the “C” arrangement of conductors to the left would quickly exceed their critical current.

There are two sources of magnetic flux from the inflector that can leak into the storage region. Because the field is produced by discrete conductors, rather than a continuous current distribution, some flux does leak out of this arrangement of conductors, see Fig. 10.6(b). The inflector lead configuration is also important, and when it was necessary to produce a second inflector, the lead configuration was changed to reduce this effect.

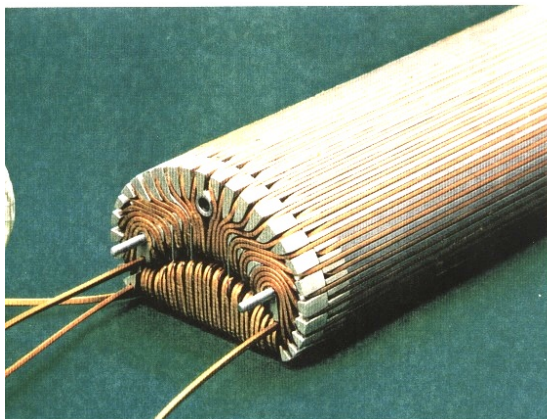
The coil was wound in two different pieces indicated by “inner” and “outer” coils in Fig. 10.6(a). One end of the coil is shown in Fig. 10.7(a) The choice was made to wind the coil over the beam channel, because this configuration would have less flux leakage, and was



(a) Inflector Conductor Arrangement

(b) Calculated Field

Figure 10.6: (a) The arrangement of conductors in the inflector magnet, showing the direction of the inflector field B_I and the main field B_0 for a beam of positive muons going into the page. The current in the inner “C” is into the page and is out of the page in the backward “D”. (b) Magnetic field lines generated by this arrangement of conductors. The beam aperture is $18 \times 56 \text{ mm}^2$.



(a) Closed Inflector End



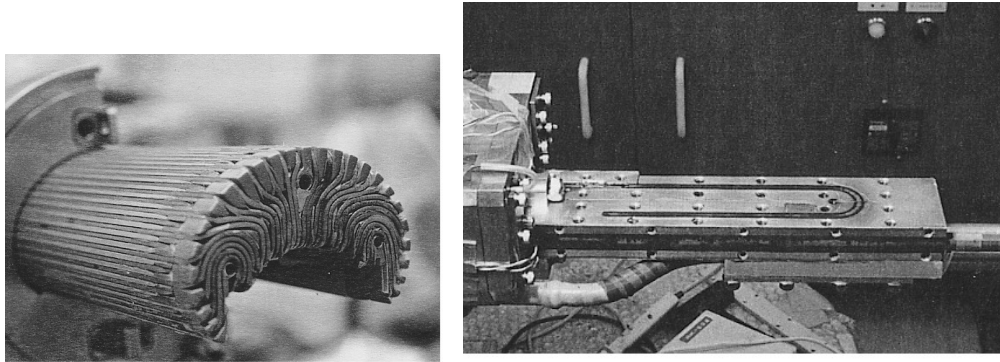
(b) Open Inflector End

Figure 10.7: (a) The prototype closed inflector end. (b) The prototype open inflector end.

thought to be more stable from quenches. However, a 0.5 m prototype was constructed with one open and one closed end, which are shown in Fig. 10.7. This prototype inflector was operated in the earth’s field, and then in an external 1.45 T field without incident.

The inner coil and the outer coil are connected in series. The joint is located inside the

downstream end of the coils; and is made by soldering the superconductors without removing the aluminum stabilizer. The joined leads were placed inside a U-shaped groove, as shown in Fig. 10.8, attached to the coil end structure. Cooling tubes run through the extender (aluminum block). One temperature sensor was mounted near the joint to monitor the local ohmic heating.



(a) Outer Inflector Coil

(b) Coil Interconnect

Figure 10.8: (a) The arrangement of conductors in the inflector magnet.(b) The joint and lead holder for the interconnect.

The geometry of the inflector cryostat is complicated by the proximity of the outer-coil cryostat, the pole pieces and the muon beam. A sketch of the beam path through the outer coil is shown in Fig. 10.9(a). The complicated arrangement where the inflector entrance nests into the concave wall of the inflector cryostat is shown in Fig. 10.9(b). Fig. 10.11 shows the combined inflector cryostat and beam vacuum chamber. The cryostat region and beam region have different vacuums, so the inflector can be cooled, independent of whether the beam vacuum chamber is evacuated.

The exit of the inflector magnet is shown in Fig. 10.14, which clearly indicates the accelerator physics issue. The incident beam is contained in the red 18 mm \times 56 mm “D”-shaped channel, while the stored beam is confined to a 90 mm diameter circular aperture. Thus it is impossible to match the β or α functions between the ring and the muon beamline without unacceptable losses in the injection channel. The result is a “ β wave” that reduces the acceptance of the ring.

10.2.2 Shielding the residual fringe field

At the design current, the maximal fringe field within the muon storage region was calculated to be about 200 G (1.4%) near the outer edge. The fringe field behaves in such a way that it is a rapidly varying function along the transverse direction, i.e. the radial direction of the storage ring, and essentially gives a negative disturbance. The fringe field of the inflector is opposite to the main field at the outer radius of the storage ring, and changes sign while crossing the central orbit.

The consequence of such a fringe field is severe. The high gradient of the field is beyond the working range of the NMR probes, so that the magnetic field map of the storage region

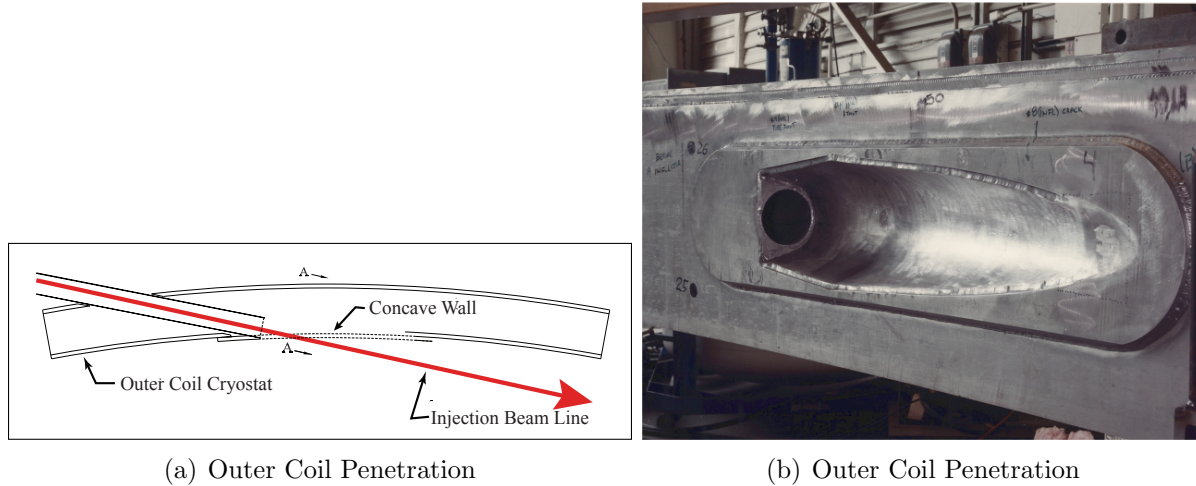


Figure 10.9: (a) A plan view of the beam penetration through the outer coil and cryostat. (b) A photo of the hole in the outer cryostat that the muon beam passes through.

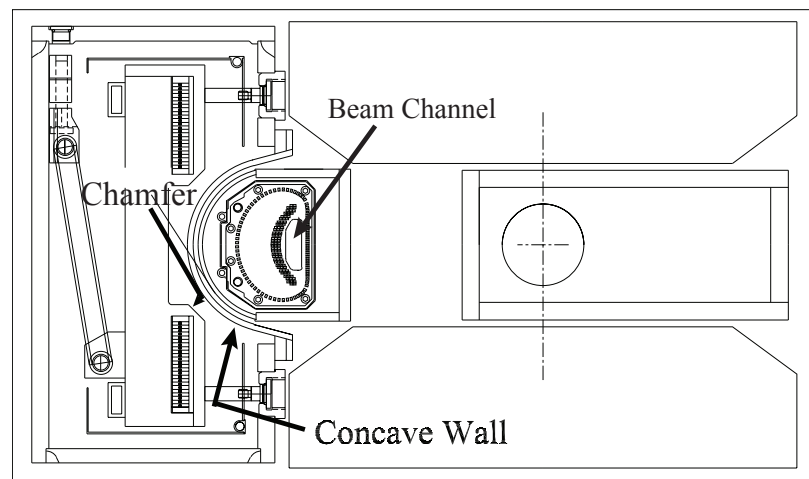


Figure 10.10: An elevation view of the inflector entrance showing the concave wall of the outer-coil cryostat where the beam exits the outer coil-cryostat.

would be incomplete, directly impacting the error of the measurement precision of the muon magnetic moment.

Conventional magneto-static shimming studies to reduce this fringe field using computer simulations were carried out. The iron compensation must be located outside the muon storage region, far from the disturbance it is trying to shield. Thus its contribution to the central field would be a slowly varying function in this space (long wavelength), which is not able to cancel the larger gradient fringe field to an acceptable level [12].

The best way to eliminate a multipole fringe field is to create an opposite multipole current source with the same magnitude. The best such current source is the super-current generated inside a superconducting material due to the variation of the surrounding field.

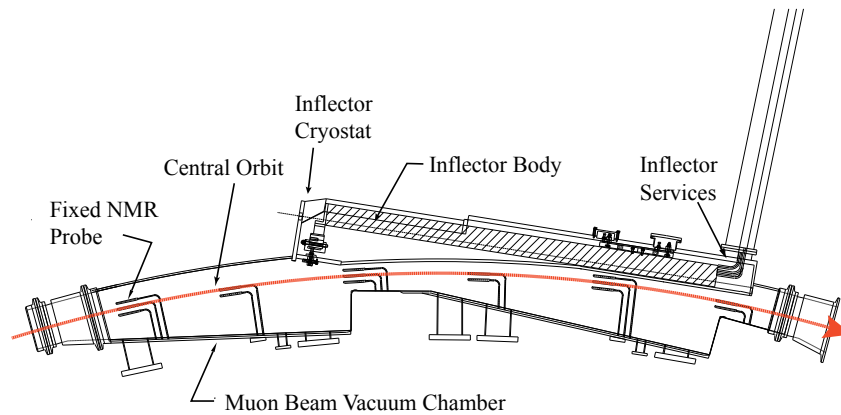


Figure 10.11: Plan view of the combined inflector cryostat-beam vacuum chamber arrangement. The inflector services (power, LHe and sensor wires) go through a radial hole in the back-leg outside of the storage-ring magnet. The NMR fixed probes are in grooves on the outside of the vacuum chambers, above and below the storage region. The red arrow shows the muon beam central orbit.



Figure 10.12: A photo of the inflector cryostat.

A method of using SC material to shield the inflector residual fringe field was studied and developed. The fringe field specification was then satisfied.

A test sheet of a superconducting shield was developed that contained 30 layers NbTi, 60 layers Nb, and 31 layers Cu. The Cu layers greatly improved the dynamic stability against flux jumping [9]. The Nb layers act as barriers, which prevent the diffusion of Ti into Cu. The diffusion could form hard inter-metallic layers and create difficulties for the rolling process. Fig. 10.15 shows the typical cross section of the sheet. Based on successful tests, Nippon Steel Corp. developed large, thin pieces of sheet especially for the $(g - 2)$ inflector, to cover

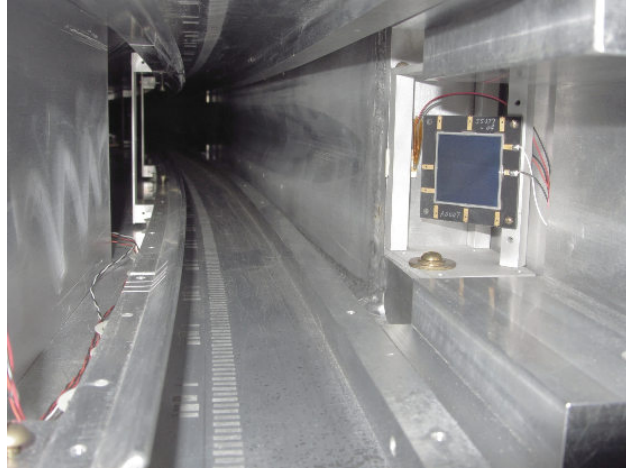


Figure 10.13: A photo of the inflector cryostat exit. A silicon detector (in blue) measured the beam profile just downstream of the inflector cryostat exit

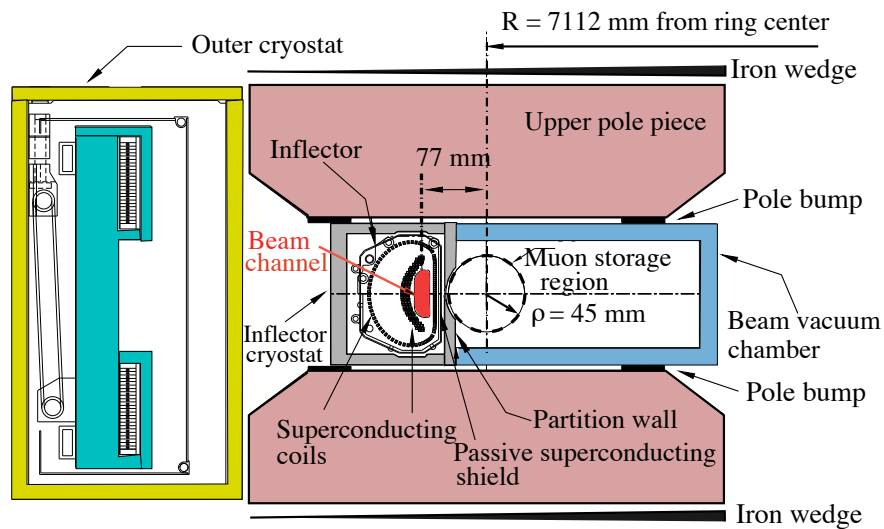
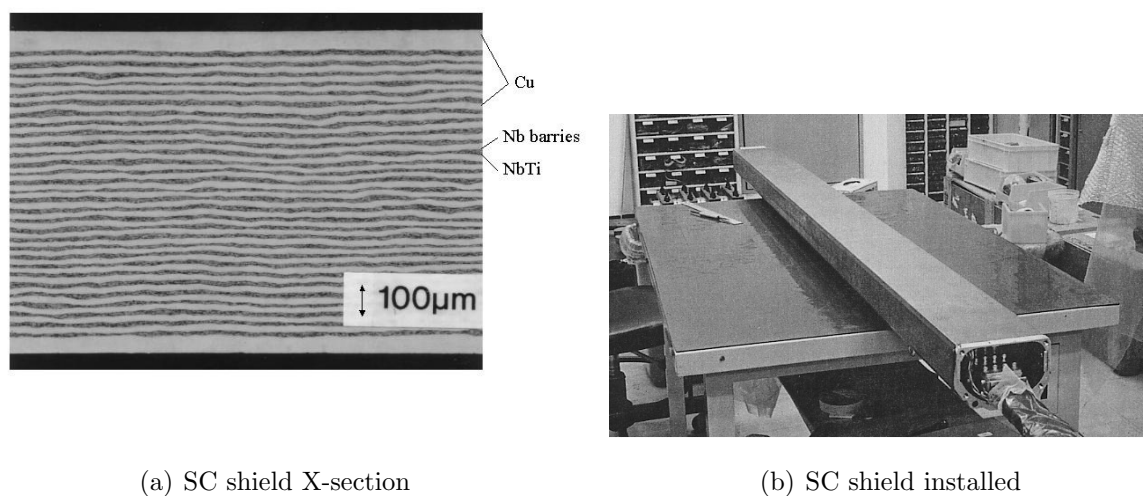


Figure 10.14: The inflector exit showing the incident beam center 77 mm from the center of the storage region. The incident muon beam channel is highlighted in red. (Modified from Fig. 9.6)

its $2 \times 0.5 \text{ m}^2$ surface and to fit into the limited space between the storage region and main magnet coil. The shielding result was extremely satisfactory.

The steps in using the shield are as follows:

1. With the inflector warm ($\sim 20 \text{ K}$) the storage ring magnet is powered and allowed to reach equilibrium.



(a) SC shield X-section

(b) SC shield installed

Figure 10.15: (a) Cross section of the multi-layer superconducting shield sheet. (b) The superconducting shield installed around the body of the inflector.

2. The inflector is then cooled to superconducting temperatures. The shield material is a Type-II super conductor, where $H_{C1} = 0.009T$ for NbTi is the maximum field for the Meissner effect to occur. Therefore, as it is cooled down to the superconducting state, the shield is not able to expel the external field. Rather, the external field will fully penetrate the shield. and the shield traps the main field.
3. The inflector is then powered. In this superconducting state, the shield will exhibit perfect diamagnetism, and will resist any change in the flux penetration through its surface.

10.2.3 Performance of the E821 Inflector

Two full-size inflectors were produced. To emphasize the importance of the superconducting shield, we relate what happened when the shield on the first inflector was damaged. In the testing of the first inflector, an accident occurred, where the interconnect shown in Fig. 10.8(b) was melted, leaving a few centimeters of undamaged cable outside of the inflector body. In order to repair it, the superconducting shield was cut to give access to the damaged superconductor. After the repair, an attempt was made to apply a patch to the shield. Unfortunately this attempt was not completely successful. The resulting fringe field reduced the storage-ring field by 600 ppm (8.7 G) over a 1° azimuthal angle, resulting in unacceptable magnetic-field gradients for the NMR trolley probes closest to the inflector body. It was also realized that a significant fringe field came from the inflector leads. A field map, averaged over azimuth, from the 1999 run using the damaged inflector, and one from the 2001 run using the new inflector are shown in Fig. 10.16. The field in the region with large gradients had to be mapped by a special procedure following data taking. This large fringe field introduced an additional uncertainty into the average field of ± 0.20 ppm (200 ppb) in the result [14]. The

1999 result had a total error of ± 1.3 ppm, so the additional 0.2 ppm uncertainty introduced by the damaged shield was small compared to the statistical error of ± 1.2 ppm. Had this error not be eliminated, its effect would have been quite serious for the 2000 and 2001 results, both of which had a total error of ± 0.7 ppm.

The damaged inflector was replaced in mid 1999, well before the 2000 running period. Two modifications were made to the new inflector design: The superconducting shield was extended further beyond the downstream end; The lead geometry was changed to reduce the fringe field due to the inflector leads. Both of these improvements were essential to the excellent shielding obtained from the second inflector.

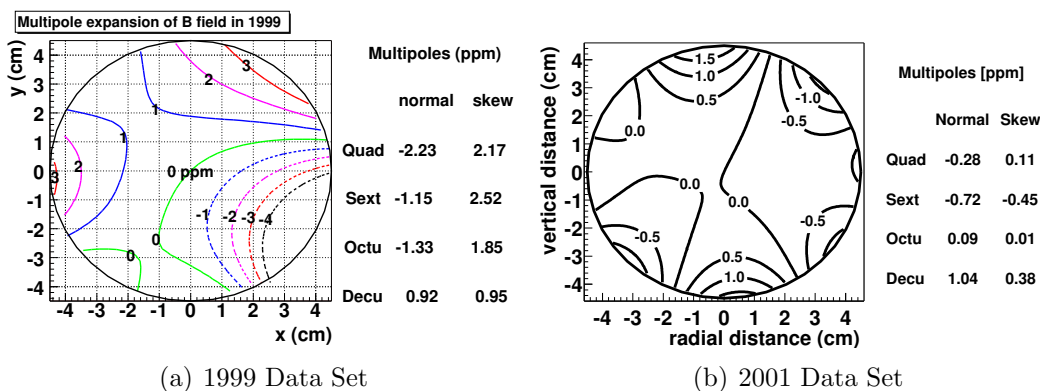


Figure 10.16: The average magnetic field $\langle B \rangle_{azimuth}$ (a) with the damaged inflector (1 ppm contours) (b) and with the second inflector (0.5 ppm contours). Note that the large disturbance in the average field was from a 600 ppm disturbance in the field over 1° in azimuth.

As with any system placed in or near the storage ring, the inflector must not disturb the magnetic field, the measurement of the magnetic field nor the distribution of stored muons at an appreciable level. The E821 inflector shield performed well but did leak some measurable amount of magnetic flux, even after the damaged inflector was replaced. Figure 10.17 shows the disturbance only minimally affects the edge of the storage volume and falls off rapidly. Except for probe 9, which is closest to the inflector, the local effect is at the $\simeq 100$ ppm level.

This disturbance must couple to a distortion of the trolley guiding rails to produce a difference between the measured field and that experienced by the stored muons. To test a worst-case scenario, we assume a local distortion of the trolley rails perfectly in phase with the field deviation due to the inflector. Fig. 10.18 shows the resultant difference in measured field compared to the true field at the position of each trolley probe, given for various amplitudes of the rail distortion. E821 achieved a precision of 0.5 mm for the trolley rails and E989 will meet this or do better (see Chapter 11). Therefore, even for an amplitude of 1 mm perfectly in-phase with the field distortion due to the inflector, the resultant systematic error is below 10 ppb across the storage volume and so the E821 inflector exceeds the magnetic field requirements of E989.

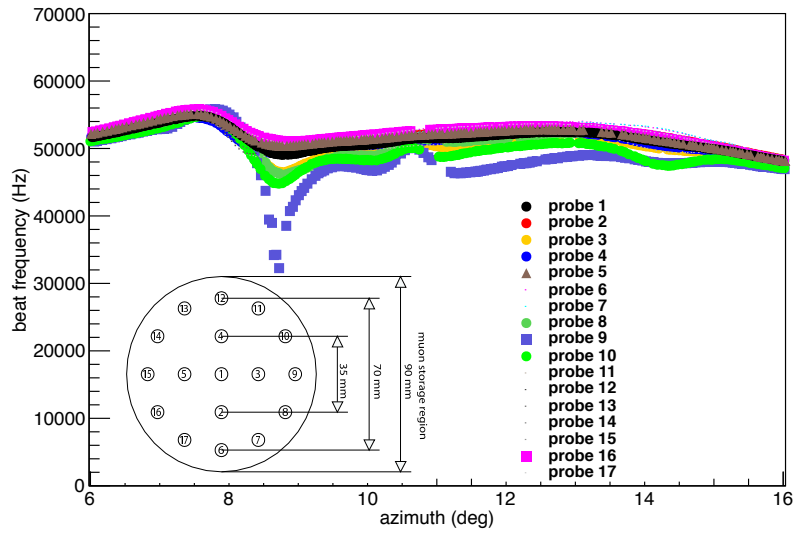


Figure 10.17: The response of the trolley probes to the second inflector fringe field during the 2001 data collection period. The insert shows the location of the trolley probes.

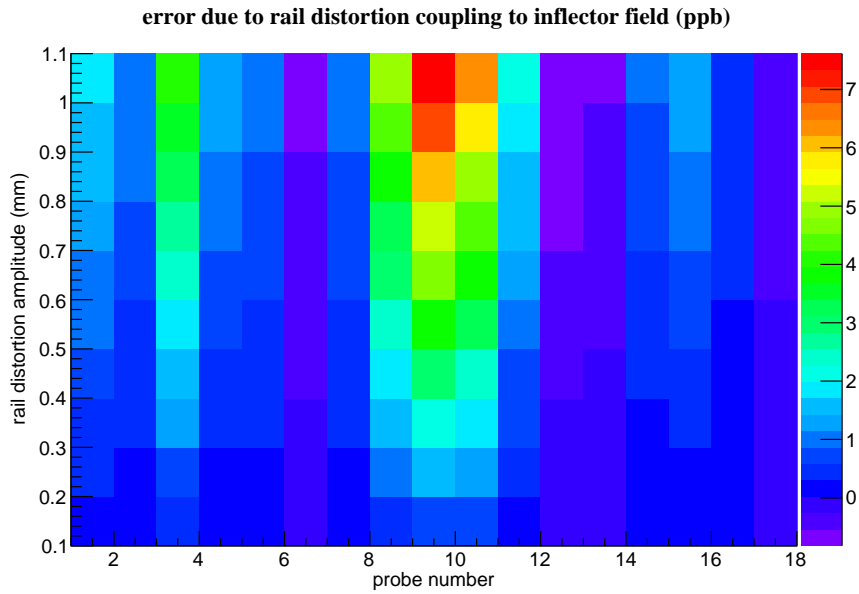


Figure 10.18: Shift in magnetic field experienced by each trolley probe for various distortions of the trolley rails perfectly in phase with the distortion of the magnetic field due to the E821 inflector. As even a 1 mm in-phase distortion of the rails causes a shift of < 10 ppb at the edge of the muon storage volume, the E821 inflector more than meets the requirements for E989.

10.3 Inflector Power Supply and Quench Protection

To power the existing inflector magnet, none of the equipment used in E821 at Brookhaven could be re-purposed. The original Transrex power supply is obsolete, as are its controls. The scenario with respect to the inflector quench detector electronics rack was the same as that for the Main Ring quench detector electronics: the components used were obsolete; no documentation exists, the PLC is obsolete; there are no spare PC boards; and there are missing cables and their documentation. We have identified a different, more modern power supply and quench protection circuit at Fermilab to re-purpose for E989.

This power supply, a PEI-150 (which is similar to the original Transrex but considerably updated in function and usability) was used as the power supply for the Dzero detector solenoid. It is presently located in the Dzero Assembly Building (DAB) and is connected to the controls, the AC power distribution, the quench protection system, and the cooling water system. Therefore, the preliminary testing was performed in its present location. The power supply and its control panel are shown below.



(a) The Power Supply



(b) Control Panel

Figure 10.19: (a) The inflector power supply. magnet. (b) Close-up of the controls.

10.3.1 Power Supply Requirements

There were two requirements given for operation of the inflector power supply: 1) the maximum DC current output must be 3500A, 2) the maximum ramp rate be limited to 2A/sec. These requirements can be met by the PEI-150 unit. Using the proper output voltage taps, the configuration chosen can provide up to 5000A at 7.5 VDC output. Using the external reference voltage input, the ramp rate can be directly controlled. In addition, this ramp rate can be limited to 2A/sec by changing some components within the PEI's control module.

Current regulation given for the unit is 0.05% (500 ppm) when operated between 20% and 100% of rated output current. Since this is a newer and redesigned version of the originally used Transrex, this regulation specification is assumed to be adequate for the inflector's operation. Like the Transrex, there is sufficient ripple at 720 Hz ripple and this ripple can approximate 20% peak-to-peak into a resistive load. This ripple is the result of the 12-phase SCR firing operation. Therefore, an external 720 Hz notch filter is connected to the output of the supply prior to being connected to the quench protection trip cabinet.

The cooling system inside of the PEI power supply is much more robust than that used for the Main Ring. Therefore, a separate regulated cooling system is not required. However, the water/coolant must be low conductivity.

10.3.2 Preliminary Testing

Once the AC service was inspected and the cooling water system reconnected, the PEI-150 power supply was powered ON. The output current was manually ramped up to 300A into the existing dump resistor. Operational voltages and controls all appear to be normal. Next, the output bus was shorted together to allow for the full operational current of 3500 A. The output current was ramped up and held at 3500A for 45 minutes. Operation appeared normal and thus completing the preliminary checkout. The power supply will remain in its present location until some operational testing using an inductive load can be performed to determine the notch filter's performance, and to determine the power supply's regulation performance. Then the power supply and components will be disassembled and moved to the final testing area where the configuration and quench protection system can be reassembled and prepared for a series of final tests for certification.

10.3.3 Inflector Quench Protection

The quench protection originally used for E821 is not documented and there was no indication of the trip cabinet arrangement. The quench energy stored in the inflector magnet (about 9 KJ), as described in Ref. [2], was not dissipated using a dump resistor but the energy was dissipated within the magnet itself. This was accomplished by turning off the power supply and using the power supply's output impedance to provide a path for the current from the collapsing magnetic field. However, given that there is only one inflector magnet available for the operation at MC-1, there was a desire to provide a more precise control of the energy dissipation in order to provide a higher degree of protection for the inflector magnet in E989.

To provide this added degree of protection for the inflector during a quench, the quench protection system is almost identical to that used for the Main Ring magnet. The only

difference is the number of tap voltages that need to be monitored. Also, a quench condition of the Main Ring magnet will be used to initiate an energy extraction from the inflector magnet.

The quench protection components, used for the Dzero solenoid, can be directly re-purposed for the inflector operation. This includes the trip cabinet with a remote-controlled reversing switch (if needed), the air-cooled 720 Hz notch filter, and the quench detector electronics rack. The quench protection circuitry, used for the Dzero solenoid and now being re-purposed for the inflector, is fully documented in ref [19]. In addition, there are existing spare modules for the controls and voltage tap input amplifiers. Only the coil voltage threshold for the generation of a quench trip signal was briefly described in ref [2]. The interconnect voltage will be set to 10 mV in consultation with Wuzheng Meng at BNL.

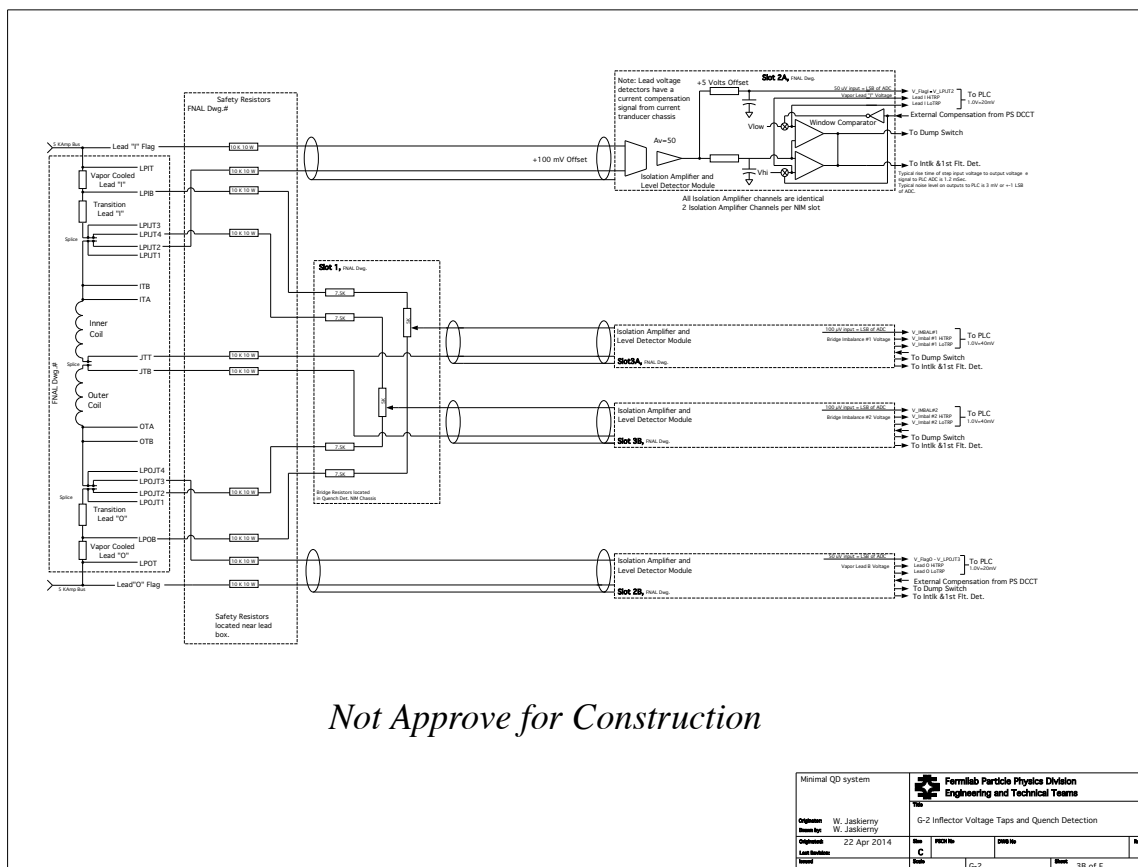


Figure 10.20: Inflector quench protection circuitry and tap locations.

In order to document the specific wiring and connector information of the inflector, a wiring schematic is being developed. According to the information at present, a draft of this schematic is shown in ref. [20]. Once verified, this schematic will be used to diagram the specific voltage taps to the connectors.

Table 10.3: Quench Protection Parameters.

Coil Voltage	120 mV
Gas-cooled lead	30 mV
Coil interconnect	10 mV

10.3.4 Power Supply and Quench Components Placement

At present, we plan to locate the inflector power supply and quench protection components within the main hall in MC-1 and also on/under the platform used for the Main Ring power supply. In E821 at Brookhaven, the power supply was located in a different room outside of the ring hall. The exact location on or near the platform will depend on the space and orientation of the components (trip cabinet, quench protection, electronics rack, etc.). The dump resistor can be placed inside or near one of the component cabinets since the estimated energy to be dissipated is quite small and should not adversely affect the MC-1 hall environmental temperature. For runs of the DC output bus that exceed 10 feet, water-cooled 10 kA bus work can be implemented to save on cost associated with the use of 535 cm locomotive cable.

One concern of locating the PEI power supply inside the main hall is the effect of 60 Hz (or multiples) magnetic fields, emanating from the power supply and the notch filter, on the Main Ring's magnetic field. An initial set of measurements were taken when the PEI power supply was operating at full output of 3500A. These measurements are currently being evaluated. If needed, magnetic shielding can be placed around the power supply to help mitigate this adverse effect, or the location of the power supply will need to be re-evaluated.

10.4 Lessons for E989 from the E821 Inflector

The most important single lesson from the E821 inflector came from the flux leakage from the damaged inflector, and the realization that the first design of the inflector leads also contributed to this problem (see Fig.10.16). The ± 0.2 ppm systematic error from this problem is three times the E989 magnetic field error budget of ± 0.07 ppm. The highly localized 600 ppm perturbation at the location of the "repaired" superconducting shield could not be shimmed away. The second issue that must be addressed is the mismatch of the E821 inflector aperture and the storage ring acceptance. The third issue is to open the ends.

The guiding principles going forward are:

- *The flux inside of the inflector must be confined inside of the inflector and not permitted to leak into the storage region.*
- *Any new inflector design must have a horizontal (radial) aperture significantly larger than 18 mm; as close to 40 mm as possible. This will facilitate beam matching into the storage ring, and should reduce the coherent betatron oscillations, and the systematic error associated with it.*

- *The ends of the inflector need to be open, rather than have coil windings across them, again to facilitate matching and to eliminate multiple scattering.*

The latter two conditions could increase the number of stored muons by almost a factor of $\simeq 2 - 3$, which would permit the measurement of a_μ^- as well as a_μ^+ .

The muon injection efficiency achieved in E821 was around 2%. Early simulations predicted that it should be 5 - 7%. Simulations by Hugh Brown showed that opening the ends of the inflector in E821 would have increased the number of stored muons by a factor of $\times 1.8$. A new open-ended inflector with a larger horizontal aperture, as large as 30 to 40 mm diameter is desirable. We are working very hard to determine how much larger the aperture can be made, given the constraints of the vacuum system and magnet geometry.

10.5 Progress Toward A New Inflector

The E821 inflector magnet was a *tour de force* in magnet design, introducing the truncated double cosine theta magnet [4] and a superconducting shield [2] that provided a constant dipole field inside of the beam channel, with flux leakage of less than 100 ppm in the region populated by the majority of the muon beam. It worked perfectly for E821, and permitted a measurement of a_μ at the 0.5 ppm level. Nevertheless, issues that would be desirable to improve in the next-generation experiment were discussed in the previous section.

Several concepts have been considered to replace the existing inflector. Any new design is constrained by the injection geometry shown in Figs. 10.1, 10.9, 10.10, 10.11 and 10.14. A passive superconducting shield to remove any leakage flux from the new inflector will be essential.

The small aperture of the E821 inflector, and the coil windings over the beam channel make matching the beamline to the storage ring impossible. Since E989 plans to accumulate 21 times the data of E821, it is necessary to revisit the inflector aperture issue. Opening the radial aperture to a 30 to 40 mm would come close to matching with the incoming beam, and permit more muons to be stored. It would also reduce the amplitude of the coherent betatron oscillations, which cause one of the significant systematic errors. As the aperture gets larger and the centroid of the injected beam is displaced radially outward, a larger kick is needed to place the beam on orbit. Shielding the flux leakage from a larger open end will also be challenging.

In E989 the knowledge of the average magnetic field needs to be improved from ± 170 ppb in E821 to ± 70 ppb. While the plan to improve the magnetic field measurement and control is discussed in Chapter 15, this plan is meaningless if any device in the experiment spoils the field by introducing extraneous magnetic flux into the storage region. The damaged inflector in E821 demonstrated how a 200 ppb problem can easily be introduced.

Two possible suggestions have been proposed for a new inflector:

- A double-cosine θ design with a larger aperture with open ends.
- A multiple coil magnet using the direct wind technology.

10.5.1 A New Double Cosine θ Magnet

We have been studying this option with our colleagues in the Fermilab Technical Division. The truncated double cosine θ design encased in a multi-layer superconducting shield worked well in E821, albeit with the limitations discussed above.

The muon beam injection into the g-2 storage ring and the storage ring operation strongly depends on the inflector magnet performance. The magnetic design for the E821 inflector was carried out by W. Meng [3], and the engineering was done by the KEK-Tokin Company collaboration in Japan led by Akira Yamamoto. This inflector will be used during the first phase of experiments at FNAL. Nevertheless, it is very desirable to build the new inflector magnet with improved performance. The new magnet should have open both ends for the muon beam, and with an increased horizontal aperture. It should be noted that it is very difficult to improve the E821 magnet design, which was based on number of models, and cold tests. The old magnet geometry and parameters with closed ends are shown in Fig. 10.21 and Table 10.4

The E821 inflector used a unique NbTi superconducting shield made by Nippon Steel, Japan [2]. It is unclear at this time whether such multilayer superconducting shield production technology still exists. Other issues are that there is no full set of inflector magnet drawings because the Tokin Company went out of business some years ago. The available space for the magnet cold mass is very constrained and cannot not be increased without major changes in vacuum vessels, thermal shields, supports, etc. So, the following action items were chosen to proceed with the first step of the magnet design and fabrication:

- Disassembly of the damaged and repaired E821 inflector magnet with the intention to use most of magnet parts.
- Measure the parts' dimensions and produce the set of cold mass drawings.
- Wind inner and outer magnet coils using copper or superconducting cable into slots of old magnet aluminum mandrels. The coil ends should have an open configuration
- Make fringe field magnetic measurements of inner and outer coils assembly at room temperature.

Now the magnet is fully disassembled (See Fig. 10.22) and the magnet components are shown in Figs.10.23 - 10.25. After disassembly, most of the parts can be used again for the magnet modeling. The main goal for this model is to verify the coil winding technology with open ends obtaining reasonable end fringe fields. The first 3D magnetic field simulation results showed that for the open ends (See Fig. 10.26) the peak field on the superconducting shield could be larger than specified shield peak value 0.1 T obtained for the magnet with closed ends.

The main reason for the larger field on the shield is the vertical bends of superconductor on both ends which generate the large normal field component in the shield area. The optimization of the superconductor bends is the most critical issue for the open end magnet approach.

The second step in the new magnet design will be the magnet cross-section optimization to increase the magnet aperture in the horizontal direction. First simulations showed that

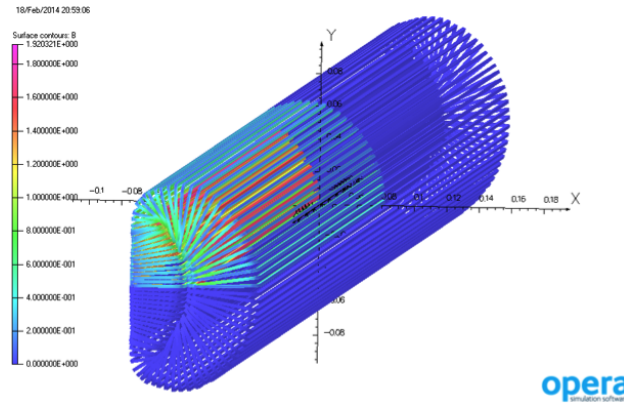


Figure 10.21: The E821 inflector coil geometry. $B_{\max} = 1.92$ T without an external magnetic field of $B = 1.45$ T

Table 10.4: Parameters of E821 inflector.

Parameter	Units	Value
Dipole magnetic field in the beam pipe center	T	1.45
Magnet effective length	mm	1696.4
Coil length	mm	1700
Total length	mm	2045
Beam pipe width x height	mm	18 x 56
NbTi superconducting screen width x height	mm	103.2 x 154.6
NbTi superconducting screen length	mm	1931
Coil current	A	2850
Superconductor with Al stabilizer bare dimensions	mm	2 x 3
Superconductor ratio (NbTi:Cu:Al)		1.0:0.9:3.7
Superconductor critical current at 3.5 T and 4.6 K	A	3890
Inductance	mH	2.0
Stored energy	kJ	9.0
Overall cold mass dimensions	mm	110x150x2025

the 10 mm aperture width increase at the same cold mass outer dimensions increases the peak field at the inner coil (the leftmost layer of the “C” shaped conductor arrangement in Fig. 10.6(a)) from 3.3 T to 5 T during the magnet operation in the 1.45 T background field from the main storage ring magnet. This is why the superconductor should have a much larger current carrying capacity at larger fields than for the E821 design. Because the E821 magnet stored energy of 9 kJ is rather low, it is possible to increase the volume of superconductor in the cable relative to the volume of copper stabilizer.

In the next section, we discuss the development of a new NbTi cable “six around one” with six NbTi strands around the central copper strand. This cable is capable of carrying a much larger current than the aluminum stabilized ASTROMAG conductor used in the present inflector. The superconducting cable grading could reduce the total volume of su-

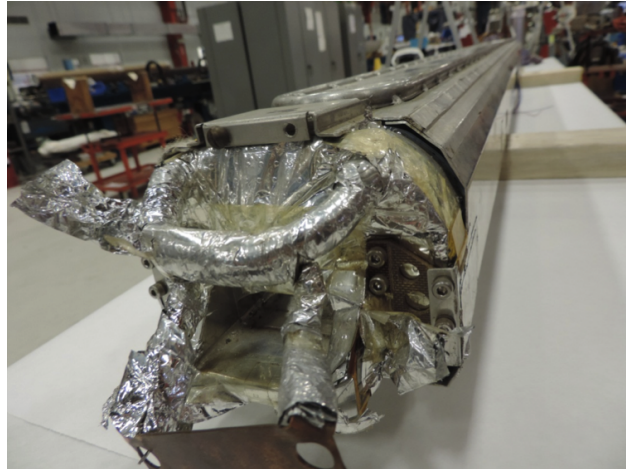


Figure 10.22: Inflector magnet cold mass with the thermal shield before disassembly.

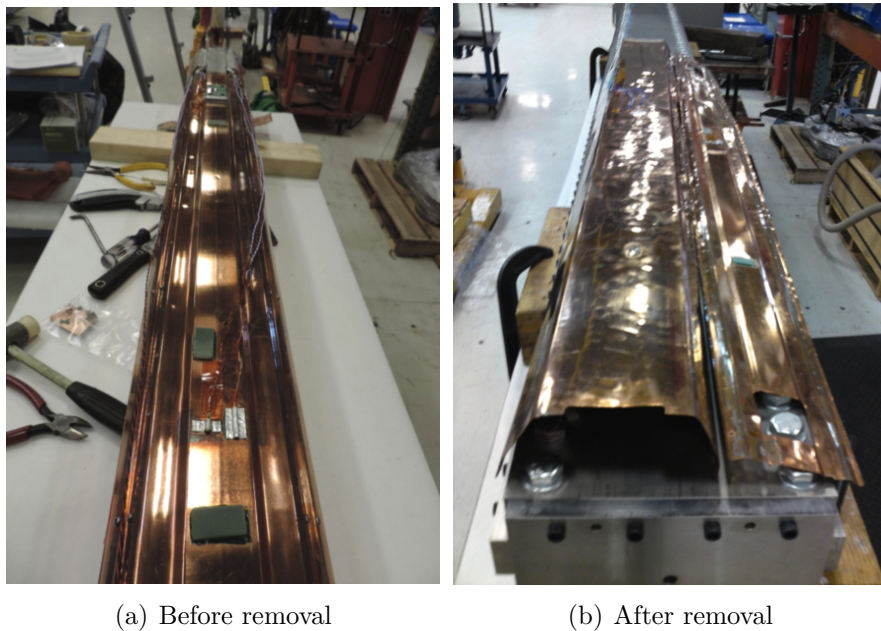


Figure 10.23: (a)The superconducting shield before (a) and after (b) removing it from the magnet.

perconductor when the outer coil will be wound with the larger cable than the inner one. Two different cables have been investigated: six around one with 0.806 mm strand diameter for the inner coil and 1.0 mm strand for the outer.

The inflector magnet has a very tight specification for the fringe field leakage into the storage ring aperture. The main ring correction system would be designed to correct the average integrated field but is not capable of correcting local field distortions. To correct these local effects we propose to use correction coils made on the base of printed board

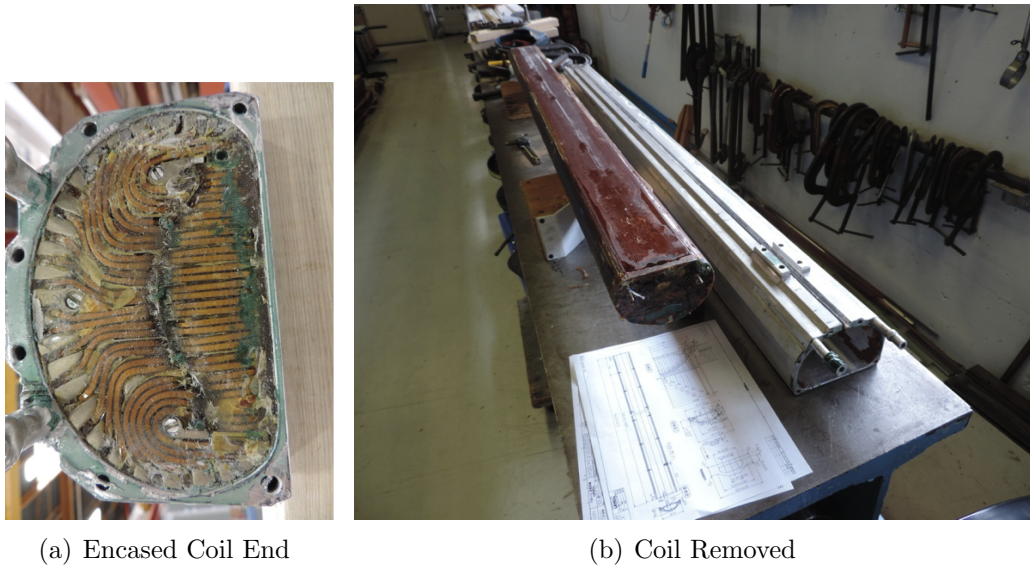


Figure 10.24: (a) View of the magnet end. The coil block was epoxy impregnated inside the aluminum case. (b) Coil block removed from the aluminum case.

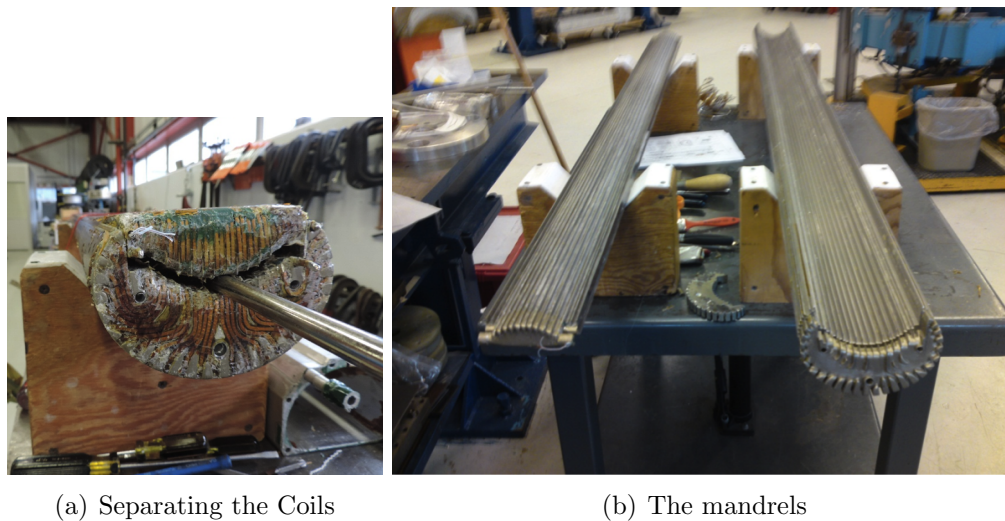


Figure 10.25: (a) Separating the inner and outer coils (b) Inner (left) and outer (right) coils aluminum mandrels after removing the superconductor from slots.

technology. For example to correct 100 ppm field distortion, requires a printed circuit board with 10 A total current. These correctors could be mounted on the pole tips or on the vacuum vessel walls.

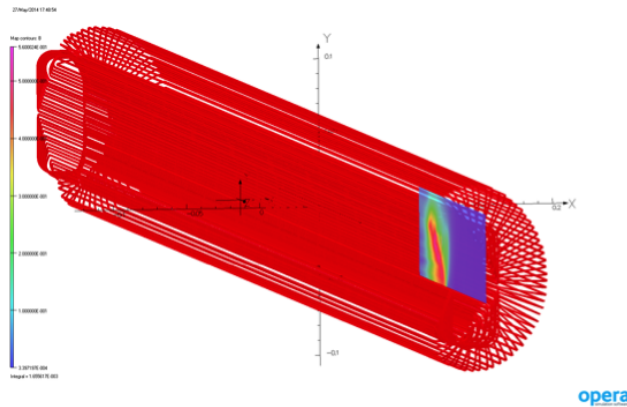


Figure 10.26: The inflector magnet with open ends. The shield peak field is 0.56 T.

Development of Superconductor for a New Inflector

In the present double cosine theta design, the operating current of the inflector is 2,685 A. The conductor of the original inflector had bare dimensions of 2 mm \times 3 mm. In an optimized design for the new inflector, a Cu stabilized conductor has been developed aiming at a similar conductor size. This was done using the Cabling Facility of FNAL's Technical Division. This facility includes a compact cabling machine with 42 spools and electronic synchronization for lay angle control, a re-spooler, sets of forming fixtures, mandrels and measuring devices, and has been mostly used to develop and fabricate wide Rutherford-type cables for dipole and quadrupole accelerator magnets. To fabricate the small cables required by the new inflector design, the idea was developed of flat-rolling a composite round cable, or 6 around 1, made of seven 0.8 mm wires. This was done to assess the feasibility of a rectangular cable of appropriate size without the need of a mandrel. Cu wires of 0.8 mm diameter were used for practice. The transverse deformation was applied with the turk-head of the cabling machine. The turk-head forming fixture is composed of two vertical rolls \sim 20 mm wide and two horizontal rolls 1.2 mm thick, both with variable gaps (see Fig 10.27(a)). Because the minimal horizontal gap presently allowed by the machine was larger than the desired cable width, the 6 around 1 cable was free to expand laterally under compression, as shown in the schematic of Fig. 10.27(b).

Using this technique, Cu cable samples were produced as shown in Table 10.5 in order to optimize the various parameters into play. These include cable pitch length (the shorter, the more compacted and rigid is the cable), thickness (the smaller, the more compact and mechanically stable is the cable), width, tension of the central wire and of the peripheral strands (not shown in Table), absence of crossovers (i.e., two strands crossing each other), and amount of residual twist produced within the cable (the lower the better). A picture of a good quality cable is shown in Fig. 10.28.

The next step was that of producing superconducting NbTi cable to measure the effect of plastic deformation on the strand superconducting properties. A 0.804 mm wire with Cu/SC Ratio of 1.34 from Oxford Superconducting Technology was used from TD inventory. The 6 around 1 cable parameters obtained with the Cu were used as starting parameters for the

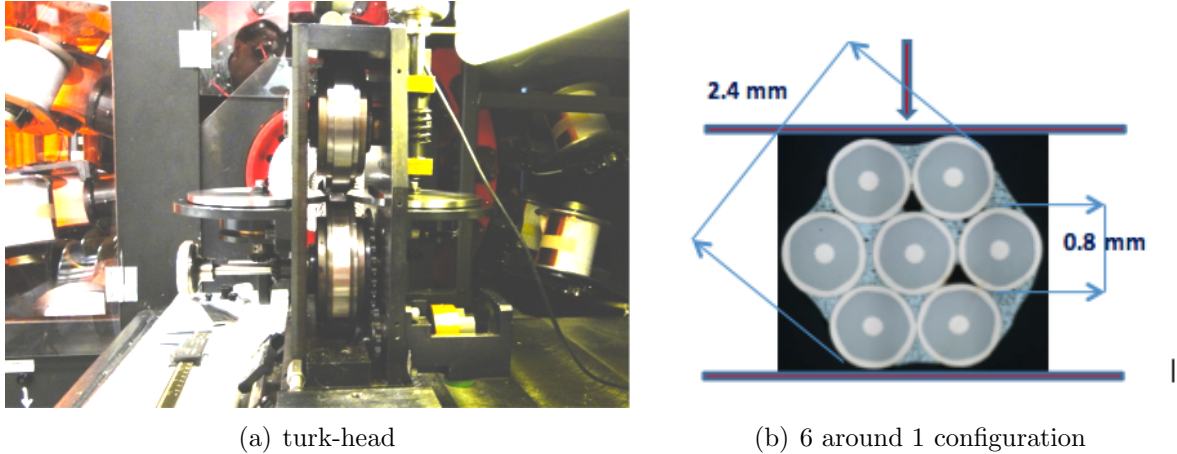


Figure 10.27: (a) Picture of the whole turk-head (b) 6 around 1 cable configuration shown with a schematic of the two compressing vertical rolls of the turk-head magnet.

Table 10.5: Parameters of the 6 around 1 cables produced out of Cu wires of 0.8 mm size.

Cable ID	Pitch length, mm	Thickness under tension, mm	Width under tension, mm	Crossover	Appearance	Inherent twist	Top roller, mm
R&D_CF_01_14 Id 1	60.0	2.4	2.4	no	good	round	0.900
R&D_CF_01_14 Id 1A	60.0	1.257	4.1	yes	very compressed	no	-0.006
R&D_CF_01_14 Id 2	40.0	1.375	3.5	no	very compressed	no	-0.006
R&D_CF_01_14 Id 3	51.8	1.35	3.71	no	good	no	-0.006
R&D_CF_01_14 Id 4	60.0	1.36	3.73	yes	center strand slightly exposed	no	-0.006
R&D_CF_01_14 Id 5	55.9	1.354	3.61	no	center strand slightly exposed	no	-0.006
R&D_CF_01_14 Id 6	transitional	section					0.300
R&D_CF_01_14 Id 7	55.9	1.72	3.75	no	good	slight	0.300
R&D_CF_01_14 Id 8	55.9	1.56	3.43	no	good	no	0.150
R&D_CF_01_14 Id 9	55.9	2.5	2.5	no	good	round	0.900
R&D_CF_01_14 Id 10	55.9	1.273	4.05	slight	fair	no	-0.006
R&D_CF_01_14 Id 11	9.0	2.605	2.605	no	poor	round	0.900
R&D_CF_01_14 Id 12	9.0	1.375	3.6	no	poor, very compressed	yes	-0.006



Figure 10.28: Picture of good quality 6 around 1 cable with thickness of 1.72 mm.

NbTi cables, which then required their own optimization since the mechanical properties of multifilamentary NbTi are very different than for the Cu. Superconducting cable samples were produced aiming at various thickness values, as listed in Table 10.6.

Table 10.6: Parameters of the 6 around 1 cables produced with seven NbTi wires.

Cable ID	Pitch length, mm	Thickness under tension, mm	Width under tension, mm	Thickness, mm	Width, mm	Crossover	Appearance	Inherent twist	Top roller, mm	0.8 NbTi outer strands	Center strand	To be tested
R&D_CF_02_14 Id 1	55.9	1.497	3.28	1.56	3.45	no	good	yes	-0.206	6	NbTi	Y
R&D_CF_02_14 Id 2	60.6	1.771	3.14	1.875	3.27	no	good	yes	-0.115	6	NbTi	Y
R&D_CF_02_14 Id 3	60.6	2.51	2.51	2.51	2.51	no	good	round	0	6	NbTi	

The critical current I_c of strands extracted from the cables above was tested at 4.2 K and up to 5 T. Some of the results are shown in Fig. 10.29, which also pictures the cross sections of cables Id1 and Id2 from Table 10.7. In these NbTi cables, the central strand suffered much less than the outer strands, which showed instead considerable I_c degradation and very low n-values, which is an indication of superconductor damage as well.

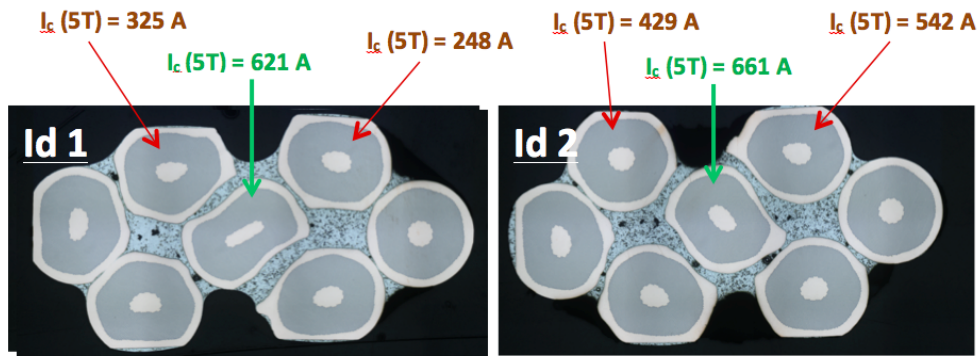


Figure 10.29: Cross sections of NbTi cables made with seven superconducting strands and showing I_c data at 5 T. (Pictures by Marianne Bossert.)

Following such results, the central superconducting strand was replaced with a Cu one, as Cu is a much softer material than NbTi, and the superconducting cable samples, as listed in Table 10.7, were produced again aiming at various thickness values.

Table 10.7: Parameters of the 6 around 1 cables produced with six NbTi wires around a central Cu strand.

Cable ID	Pitch length, mm	Thickness under tension, mm	Width under tension, mm	Thickness, mm	Width, mm	Crossover	Appearance	Inherent twist	Top roller, mm	0.8 NbTi outer strands	Center strand	To be tested
R&D_CF_03_14 Id 1	60.6	2.40	2.40	2.40	2.40	no	good	round	0	6	Cu	
R&D_CF_03_14 Id 2	60.6	1.785	3.23	1.865	3.25	yes	fluffy	yes	-0.112	6	Cu	Y
R&D_CF_03_14 Id 3	40	1.713	3.13	1.800	3.16	no	good	yes	-0.112	6	Cu	Y

The critical current I_c of strands extracted from the cables above was tested at 4.2 K and up to 5 T. In these NbTi cables with a central Cu strand, the latter absorbed most of the deformation, therefore better preserving the integrity of the outer NbTi wires. This is shown in Fig. 10.30, which also pictures the cross sections of the cables from Table 10.7. This can also be seen from Fig. 10.31, which demonstrates how the cable with only 6 NbTi strands and 1.8 mm thickness performs better over all of the magnetic field range and offers more Cu stabilizer than the 100% NbTi cable, despite the latter being thicker at 1.875 mm, but suffering more damage and therefore seeing larger critical current degradation.

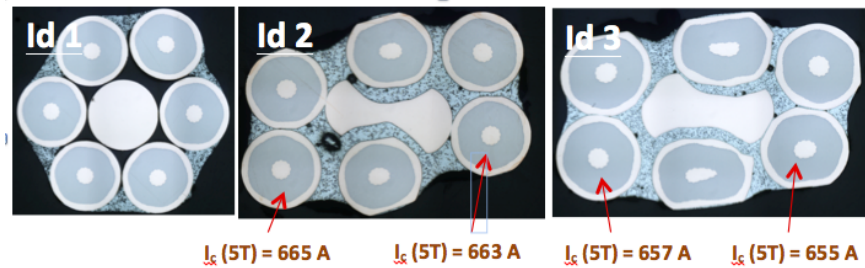


Figure 10.30: Cross sections of NbTi cables made with six superconducting wires around a central Cu strand and showing I_c data at 5 T. (Pictures by Marianne Bossert.)

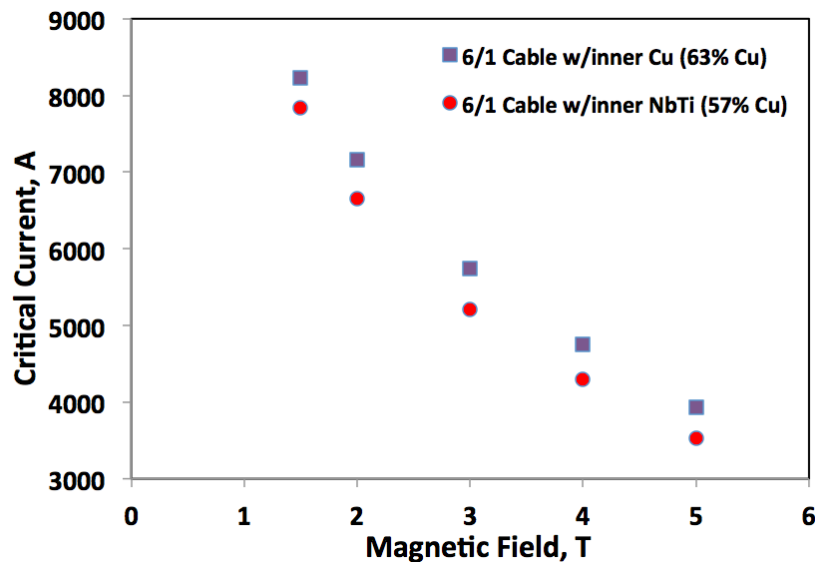


Figure 10.31: I_c as a function of magnetic field B for the 6 around 1 cable made with only NbTi strands and that made with a central Cu wire.

The cable performance at the inflector operation temperature of 4.6 K is obtained by parameterizing and fitting the data acquired at 4.2 K. At 4.6 K and at the maximum field of 3.5 T seen by the inner layer of the magnet under design, the 6 around 1 cable made of six NbTi wires around a central Cu strand is expected to carry 4,800 A, which offers 80% margin with respect to an operation current of 2,685 A. A length of 60 m of such 1.8 mm \times 3 mm cable was fabricated for magnet practice winding, and a length of round cable, which is sufficient to wind the whole magnet (i.e. 170 m), was also fabricated. This latter cable will be available to be used as-is if needed, or to be flat-rolled to size, according to the feedback produced by the practice magnet winding. Constraints associated to the winding technology will determine whether further cable R&D will be needed (for instance if cable twist were to be considered excessive for winding, solutions would have to be proposed).

To accommodate instead an inflector magnet design with 10 mm larger aperture, which produces a larger maximum field of 5 T on the outer coil, a similar 6 around 1 study was

carried out using 1 mm NbTi and Cu wires. The results on the effect of the central softer Cu wire were very similar for all the produced cables, which again aimed at various thickness values. The superconducting properties of the NbTi peripheral strands were preserved with very good I_c retention with respect to the virgin wire. Based on extracted strands I_c data, a cable of 2.3 mm \times 3.85 mm is expected to carry 4,800 A at 5 T and 4.2 K. A sample of the latter cable was produced for magnet practice winding of the outer layer.

10.5.2 The Superconducting Passive Shield

For any given magnetic field value B_1 to be shielded by a superconducting slab exposed to an external magnetic field B_{ext} (see the schematic in Fig. 10.32), the thickness d_{min} that is requested of the slab is inversely proportional to its critical current density, $J_c(B_{ext})$, according to the following simple formula:

$$d_{min} = \frac{B_1}{\mu_0 J_c} \quad (10.1)$$

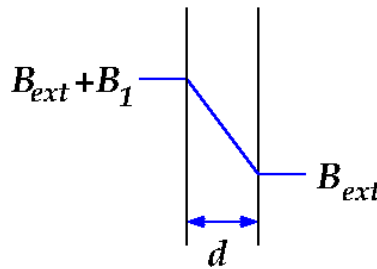


Figure 10.32: B_1 is the magnetic field value to be shielded by a slab of thickness d exposed to an external magnetic field B_{ext} .

For the shield of the inflector magnet, $B_{ext} \simeq 1.5$ T and $B_1 \geq 0.1$ T. The J_c can be obtained from either testing the critical current I_c of a superconducting sample and normalizing it to the transverse superconducting area of the sample, or from magnetization measurements. The latter are especially important for accuracy at low magnetic fields below 2 T, where self-field effects are non-negligible. This topic is expanded at the end of this section.

In order to test the critical current I_c of NbTi foil samples, an existing experimental setup of the Superconducting R&D lab in FNAL's Technical Division (TD) was modified and re-commissioned. New parts for the sample holder have been procured to replace with pressure contacts the soldered contacts between sample and electrical leads, and between sample and voltage taps. This was done since bulk NbTi cannot be soldered to Cu. The new setup is pictured in Fig. 10.33(a-b). In the middle is the transverse view of the NbTi foil sample mounted in its holder. The sample ends are coated with Indium, inserted within two circular half lugs made of Cu, and clamped to the Cu current carriers. Stainless steel screws are used as voltage taps. They are held on the sample face in its central area by means of G-10 holders, as seen on the left. This setup allows for the sample rotation to perform

critical current tests at different field orientations with respect to the sample. The I_c tests on shield samples were performed at 4.2 K from 0 T to 2 T in the parallel and perpendicular field orientations shown in Fig. 10.33(c). The samples were 3 mm wide and 38 mm long.

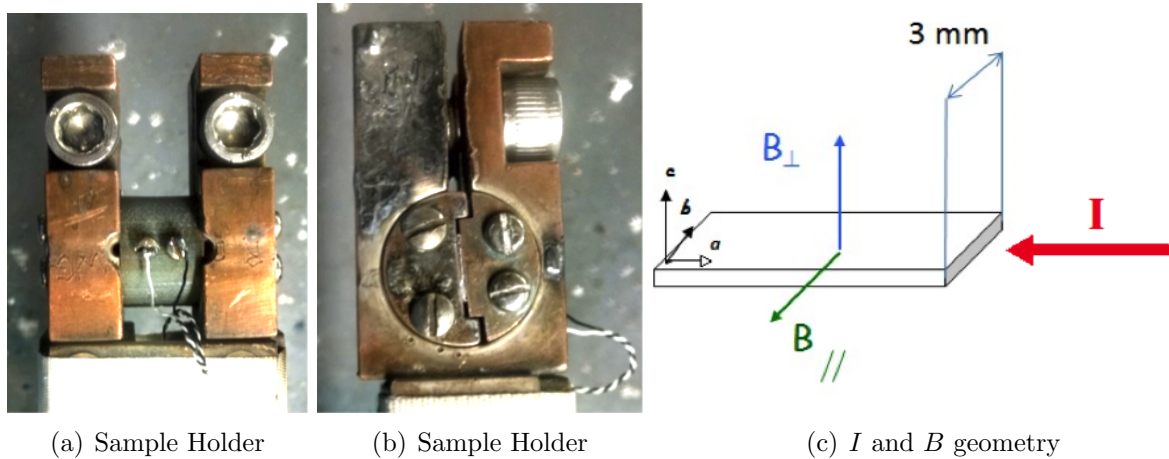


Figure 10.33: (a-b) Transverse view of a NbTi foil sample (b) mounted in its holder. The sample ends are coated with Indium, inserted within two circular half lugs made of Cu, and clamped to the Cu current carriers. Stainless steel screws, used as voltage taps, are held on the sample face in its central area by means of G-10 holders. (c) Magnetic field orientations used to test the I_c (4.2 K) of superconducting shield samples, which were 3 mm wide and 38 mm long.

Another factor to take into account for the characterization of these sheets is their I_c anisotropy. The I_c is typically the largest along the rolling direction, which is shown for instance in Fig. 10.34 for the 25 cm wide and 100 μm thick Luvata NbTi sheet. In the case of samples cut out of the Nippon Steel Corporation shield used in the first inflector, the rolling direction was unknown. In the following plots the orientation of the latter samples is therefore indicated by their cross section being transverse or parallel to the beam direction with respect to the shield location in the first inflector magnet. Also, because the Japanese shield is made of dozens of thin superconducting layers embedded in Nb and Cu, in Figs. 10.35(a-b) the engineering critical current density J_e was used to compare the performance of samples from the original shield with the Luvata samples. To obtain J_e the I_c is normalized to the total cross section of the sample.

Optical microscopy of samples from the first E821 inflector's shield confirmed that the rolling direction of the shield was that parallel to the beam with respect to its location in the first inflector magnet. This can be seen from Figs. 10.36(a-b), where in the former the superconducting layers in the cross section cut transversely to the beam are flatter and less inhomogeneous than those in the cross section cut parallel to the beam. In these same cross sections one counts 29 Cu layers and 30 intermediate NbTi/Nb layers within an overall slab thickness of 0.22 mm to 0.24 mm. This means that in the first inflector the original 0.75 mm shield developed by Nippon Steel Corporation had been used after further rolling to make it thinner.



Figure 10.34: Picture of Luvata NbTi sheet showing also its rolling direction.

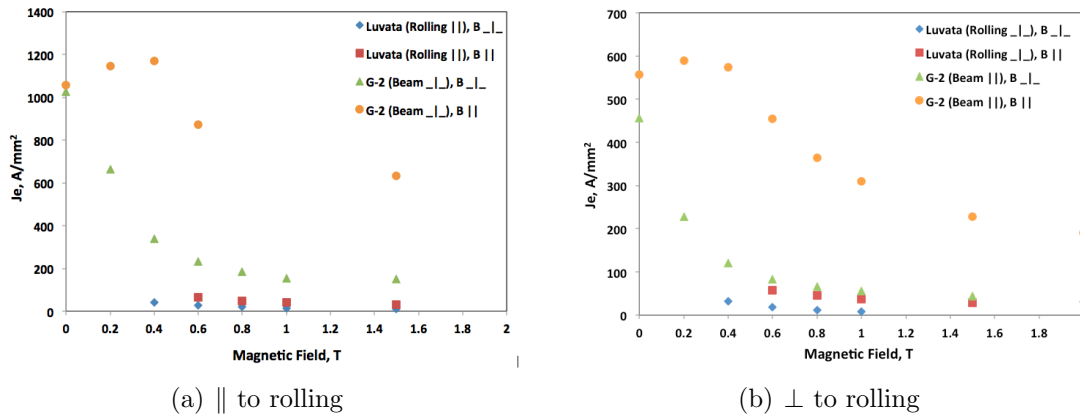


Figure 10.35: (a) Comparison of the engineering critical current density J_e along the rolling direction as function of both parallel and perpendicular magnetic fields between samples from the first inflector shield and the recently acquired Luvata samples. (b) Comparison of the engineering critical current density J_e perpendicularly to the rolling direction as function of both parallel and perpendicular magnetic fields between samples from the first inflector shield and the recently acquired Luvata samples.

The comparison study showed that in parallel field the J_c of the original Japanese shield is more than 10 times larger than the Luvata. It also showed that the original shield is strongly anisotropic, in that the difference in performance between the rolling direction and its orthogonal one is greater than a factor of 3. This can be compared to the bulk NbTi sheet by Luvata where such difference is less than 10%. The difference in performance in parallel and magnetic fields is also larger for the multilayer shield than for the Luvata slab.

As mentioned above, the J_c of a superconductor can also be derived from magnetization measurements, where a slab of thickness d is exposed to an external cycling magnetic field B , which induces in the slab two opposite and equal currents. An example of such hysteresis curve is shown in Fig. 10.37(a). The associated magnetic field profile can be seen in

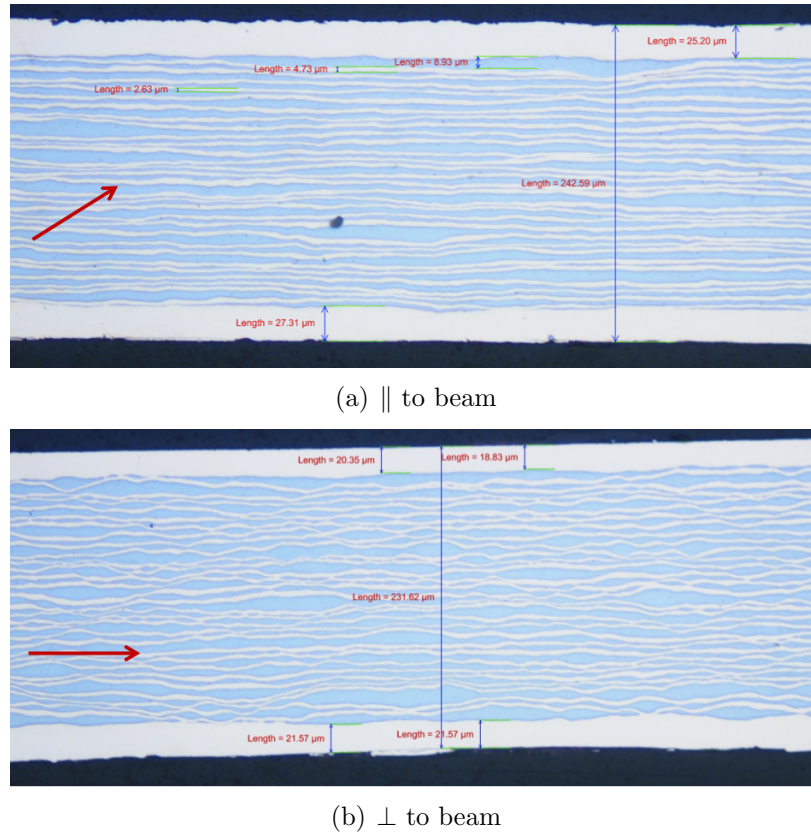


Figure 10.36: (a) Microscopy of original shield sample cut transversely to the beam (shown in Figure as entering the sheet) with respect to its location in the first inflector magnet. (b) Microscopy of original shield sample cut parallel to the beam with respect to its location in the first inflector magnet (Pictures by Allen Rusy, FNAL).

Fig. 10.37(b). The amplitude ΔM of the magnetization curve follows the following equation:

$$\Delta M = \frac{\mu_0 J_c(B) d}{2} \quad (10.2)$$

Magnetization measurements of superconducting samples are performed in TD using a balanced coil magnetometer (Fig. 10.38(a)). The sample is placed inside one of two balanced pick-up coils, and its magnetization is derived from an integrated voltage signal. These measurements are currently performed in parallel magnetic field. Using such setup, samples of the NbTi Luvata foil (Fig. 10.38(b)) of both orientations (i.e. with current parallel and orthogonal to the rolling direction) were tested at 4.2 K up to 3 T, and their $J_c(4.2 \text{ K})$ were obtained from Eq. 11.2. The J_c results at 4,2 K are shown in the plot of Fig. 10.39, where they are also compared with the J_c data obtained with transport current measurements. Below 2 T the transport current data produce lower J_c values due to self-field, and the data converge in the vicinity of 2 T.

The comparison of Eqs. 10.1 and 10.2 produces the simple following correlation for our

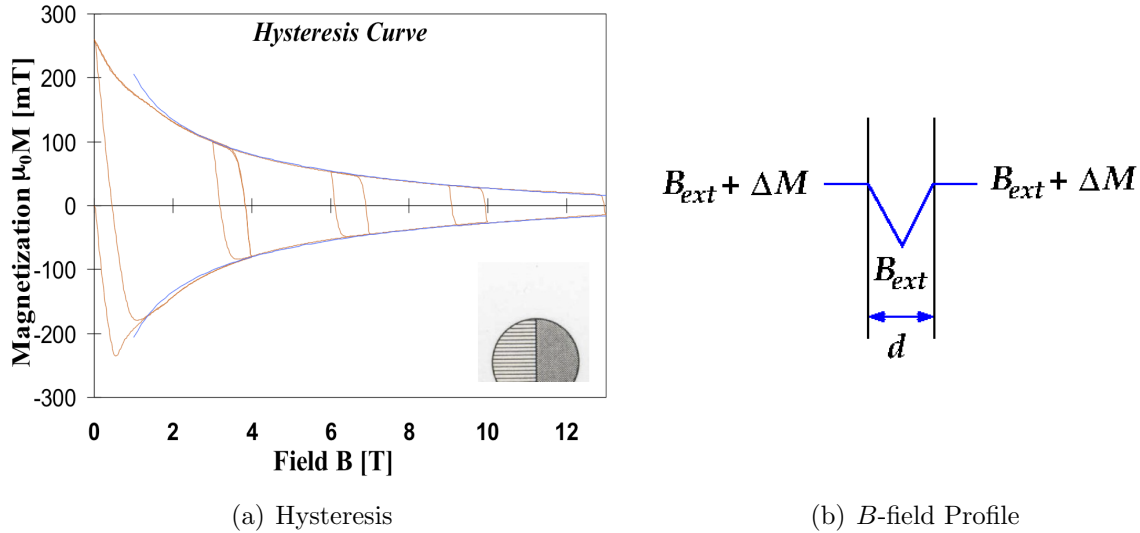


Figure 10.37: (a) Typical magnetization curve of superconducting material. (b) Magnetic field profile of superconducting slab exposed to external magnetic field.



Figure 10.38: (a) Balanced coil magnetometer used in TD to measure magnetization of superconducting samples. (b) Magnetization sample made by winding a number of turns of the NbTi Luvata foil.

experiment:

$$B_1 = 2\Delta M(B_{ext}) \quad (10.3)$$

The ΔM measured in parallel field at 1.5 T for the Luvata foil sample in the rolling direction was of 0.07 T, i.e. $J_c(1.5 \text{ T})$ 110 A/mm², producing a shielding field B_1 of 0.014 T. This is consistent with Eq. 10.1, which for superconducting slabs 100 μm thick requires a $J_c(1.5 \text{ T})$ of 800 A/mm² in order to shield 0.1 T. A shield 250 μm thick like that used in the first inflector would require a $J_c(1.5 \text{ T})$ of 350 A/mm² to 400 A/mm² to shield 0.1 T. Transport measurements performed so far in parallel and perpendicular fields respectively showed a $J_c(1.5 \text{ T})$ between 149 A/mm² and 633 A/mm² in the rolling direction, and a $J_c(1.5 \text{ T})$ between 44 A/mm² and 228 A/mm² in the orthogonal direction. More accurate values could possibly be obtained with magnetization measurements.

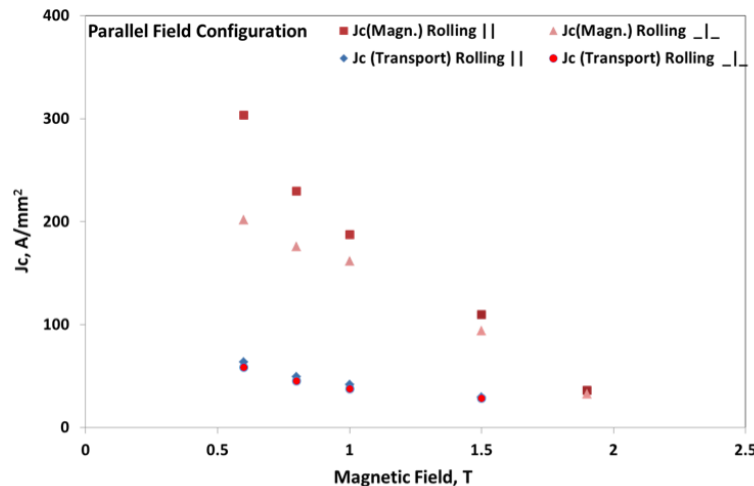


Figure 10.39: Comparison of $J_c(4.2\text{ K})$ obtained in parallel magnetic field for samples of the NbTi Luvata foil of both orientations (i.e. with current parallel and orthogonal to the rolling direction) using magnetization and transport current measurements.

10.5.3 Double Magnet, Using the Direct Winding Technique

A technique of “direct winding” of superconducting coils has been developed at Brookhaven National Laboratory by Brett Parker. The E989 project has engaged him to come up with a design of a new inflector that uses this technology. The BNL Direct Wind technique is a computer controlled magnet production process where:

- We temporarily bind round superconducting cable to the outer surface of a support structure
- Fill in empty space in the winding pattern with a combination of G10 and epoxy
- After which we apply a compression wrap of s-glass fiber under tension to provide coil pre-stress to counter the Lorentz forces on the conductor during operation.

A complete coil package usually consists of several coil layers. Since we can make small field tuning corrections in successive coil layers based upon magnetic measurements of earlier layers we have been able to satisfy challenging magnetic field quality goals. In this manner we have fabricated rather complex, compact, self-supporting coil structures for a variety of projects[26].

A seemingly natural inflector magnet configuration is one that has nested Direct Wind dipole structures that are adjusted so to have their mutual external fields cancel; however, unless these dipole coils are aligned on a common center (which increases the required kicker strength) this geometry leads to large conductor peak fields due to flux that has to be “channeled” between the inner and outer coil structures. This peak field increase could be mitigated by adding a significant defocusing gradient to the dipole field but this has other unfavorable consequences for the beam optics.

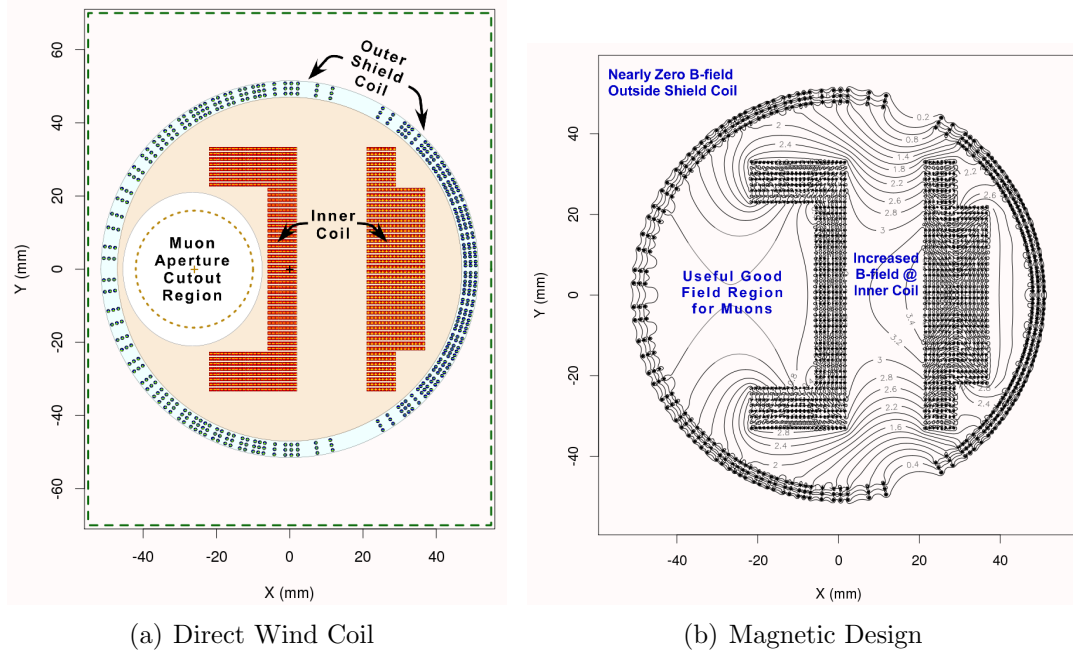


Figure 10.40: (a) Conductor Cross Section for an open end coil inflector magnet. The dipole field in the muon aperture results from the combination of the external field due to a nearby coil plus the field generated by a three layer Direct Wind shield coil. (b) Contours of Constant $|B|$ Plotted for the open end coil inflector magnet. Here we see that the B -field from the inner coil and outer shield coil is well contained within the boundary of the outer shield coil. Horizontal space is constrained so increasing the space available to the muon beam means reducing the space for flux inside the inner coil which results in increased coil peak field.

Thus in order to maximize the clear aperture for incoming muons while minimizing the increase in required kick angle we have settled upon a hybrid coil scheme shown in Fig. 10.40(a). Motivation for this scheme comes from consideration of the E821 design (see Fig. 10.6), which can be viewed as consisting of two modified dipole windings of opposite polarity placed side-by-side. The flux generated by the coil turns around the main muon aperture is augmented by the external field due to coil turns next to the main aperture. Similarly in Fig. 10.40(a) we have a side coil structure whose external field provides part of the dipole field with the rest coming from the internal field of an outer dipole shield coil; the external field of the inner coil and outer shield cancel each other outside the structure but they add coherently in the main muon aperture as shown in Fig. 10.40(b).

Because the inner coil does not have to pass the muon beam, we choose to wind it as a series of closed end, racetrack coils rather than via Direct Wind. This choice opens the possibility to use a larger and more robust (e.g. added superconductor yet also more room for copper stabilizer) rectangular conductor for winding the inner coil. The inner coil is shaped to both fit inside the shield coil and to provide improved field uniformity on the muon aperture. Reducing the space inside the inner coil gives more space for the muons

on the outside at the cost of raising the peak field at the inner coil; however, with its inner conductor having increased operating margin, this is tolerable especially as the inner coil closed ends helps to keep field contained inside.

The inner coil is wound on a solid structure with integrated cooling channels so that the conductors are well supported and conduction cooled. When assembled with some additional parts we come to a smooth outer surface around the inner coil structure upon which we can lay down a three layer Direct Wind coil structure using round cable. Before winding each of the shield layers we make magnetic measurements of the field generated by what has been wound so far and compare to our calculated expectations. In this manner we can derive small corrections before winding each successive shield coil layer to ensure that when the inner coil and external shield coil are powered in series that the external field is canceled as well as possible.

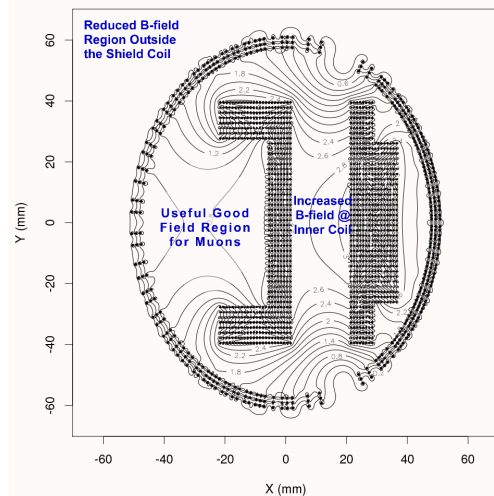


Figure 10.41: Contours of constant $|B|$ plotted for vertically expanded inflector magnet. Here we have the same basic coil structure as for Fig. 10.40 except that all vertical dimensions have been expanded by 20% resulting in 20% greater vertical aperture for muons. The field extending beyond the shield coil is small and it is anticipated that it could be reduced further with minor re-optimization of conductor positions.

Preliminary estimations based upon field calculations of the middle (effectively 2d) section of the inflector magnet indicate that it is possible to keep the external field in the middle well below levels acceptable for the passive superconducting shield. Optimization of the coil “ends” is currently in progress and we do not yet have results available to what level the inflector end field components can be suppressed before reaching the superconducting shield. However we anticipate that a combination of tailoring the end field of the shield coil, as has been successfully demonstrated for the SuperKEKB cancel coils [27], will be necessary along with moving some fraction of the inner coil turns out of their racetrack planes (in a manner similar to making “bedstead turns”) in order to truncate the coil end field to an acceptable level. This is the main remaining design optimization task upon which work will continue.

We will also investigate manufacturing a non-circular shield coil as shown in Fig. 10.41. The configuration shown in Fig. 10.41 comes from stretching the previous round configuration by 20% vertically. The benefit of the stretched configuration is gaining 20% in vertical aperture to be able to transport more muons. However, in both theory and practice optimizing the coil configuration for non-circular coils and deriving winding pattern corrections from magnetic measurements is much more complex, so that there is increased risk that the production magnet would have significant field errors. At this point in time completing the end field optimization for circular coils is of highest priority but once completed it will be natural to extend the optimization to include non-circular coils.

10.6 Muon Storage Simulations Using a New Inflector

Several aspects of a new superconducting inflector magnet are simulated¹ to study their impact on the fraction of muons transmitted into the storage region. There is significant ongoing work on simulations, and this report summarizes progress to date. Initially studies focused on the E821 inflector, and the beam that could be stored using it at Fermilab. As the end-to-end beam has been developed, these calculations have become more sophisticated. The information presented below represents our latest, but not final results. While promising, it is very much a work in progress. Simulations for E821 predicted that an inflector with open ends (and 18 mm horizontal aperture) would store 1.75 times as many muons as one with both ends closed.

The latest simulation begins with protons hitting the production target, the creation and decay of pions, and propagation of the muon beam around the delivery ring and into the muon storage ring. The temporal distribution of the muons is assumed to be the same as that of the protons on target, with base width of 120ns. There are 10,000 muons in the distribution. The kicker field profile is for the E989 plate geometry, and the kicker pulse is assumed to have 20 ns rise and fall times with 80 ns flat top. The distribution of muons is tracked through the hole in the backleg iron, the storage-ring fringe field and through the inflector. The simulation includes scattering in the upstream cryostat window, and the coils on both ends of the inflector. The downstream cryostat window is not included. There is scattering in the quadrupole plates as the muons enter the storage ring. The quadrupole plates are assumed to be in the E989 geometry, with the short plates in Q1 at the nominal 5 cm radius from the beam center, and the longer plates at 7 cm. The results from the most recent simulation are shown in Fig. 10.42.

The red curve shows the capture efficiency as a function of kicker field for the baseline inflector configuration. The error bars are statistical. β_x , β_y , and η_x have all been optimized for capture efficiency using similar scans. For each set of Twiss parameters the distribution is “refocused” upstream of the magnet iron so that it will have the desired phase space parameters in the inflector. That is, the β -functions in the inflector are optimized for capture efficiency.

The green curve corresponds to the case where the overlapping inflector end coils are eliminated but with no change in aperture. To estimate the benefit of a larger inflector bore we increase the aperture of the inflector to ± 18 mm from ± 9 mm (blue curve) (and

¹This material complements the discussion in Section 8.3.2

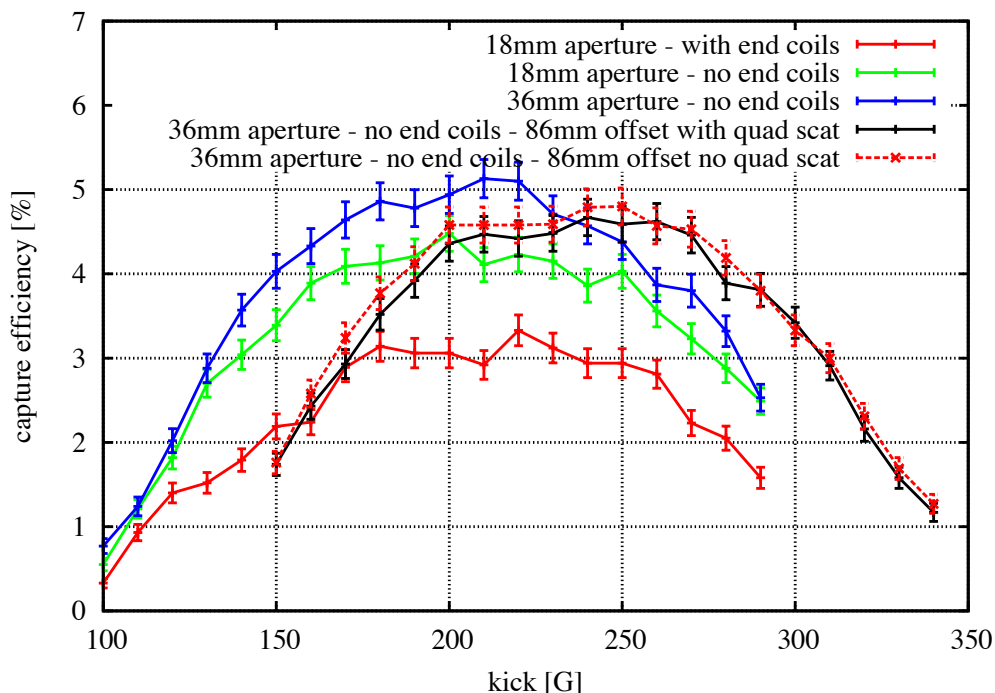


Figure 10.42: Capture efficiency vs kicker magnetic field. The red line (18 mm aperture with end coils) represents the baseline design using the E821 inflector.

eliminate scatter in the end coils). This is a bit artificial since it assumes no change in the radial position of the inflector axis (see Fig. 9.6). The black curve assumes that the inflector axis is displaced radially by $77 + 9 = 86$ mm and we find that the optimum kick field increases. To see if the reason that with the 86 mm offset (black) was worse than the 77 mm offset (blue) was caused by scattering in the quadrupole plates, the quadrupole scattering was turned off, which gave the dashed curve; a small effect. At present it is not clear why the efficiency is worse for the case with the 86 mm offset compared to the 77 mm offset. We are continuing to study this effect to determine its source.

10.6.1 E821 Inflector Simulation

In this section we report on the earlier studies. We are actively comparing these results to the recent one discussed above. The options studied were the following with the E821 setting shown in parentheses: *a*) open-end vs closed-end (E821) geometry, *b*) 40 mm vs 18 mm (E821) horizontal aperture, *c*) sensitivity to beam phase-space matching. Results of the simulation are presented as improvement factors defined as the fraction of stored muons with the new inflector divided by the baseline E821 inflector. The baseline E821 storage rate

is also presented. Assuming all improvements add coherently, a new open-ended inflector with a 40 mm horizontal aperture is expected to increase the fraction of stored muons by a factor of 3.8 compared to the E821 inflector.

The E821 inflector magnet is simulated using a GEANT-based software, which allows particle tracking beginning at the upstream end of the inflector. Within this framework, the closed ends of the inflector are constructed using distinct volumes of aluminum (1.58 mm), copper (0.39 mm), and niobium-titanium (0.43 mm). An additional 4 mm of aluminum is added to each end to model the window, flange, and cryostat. Between the end-caps, a “D”-shaped vacuum beam channel is constructed to approximate the double cosine theta geometry. The magnetic field within the beam channel is the vector sum of the main magnet fringe field and the 1.45 T field ($\int \vec{B} \cdot d\vec{\ell} = 2.55 \text{ Tm}$) produced by the inflector magnet.

The E821 muon beam is simulated by uniformly populating a 40π phase space ellipse. The phase space axes are determined by the beam Twiss parameters, α and β in both horizontal (x) and vertical (y) directions. The nominal Twiss parameters are determined by maximizing the transmission rate through the inflector and shown in Table 10.8 when the beam is localized at the “downstream”-end of the inflector (*i.e.* nearest to the ring). The beam momentum, $|P|$, is generated by sampling a Gaussian distribution with mean equal to the magic momentum P_{magic} and width $\delta P/P = 0.5\%$. The longitudinal width of the beam, or equivalently the width in time, is 25 ns.

Table 10.8: Nominal muon beam Twiss parameters.

Direction	Emittance (ε)	α	β
Horizontal (x)	40	-0.544	2.03
Vertical (y)	40	-0.0434	19.6

All muons passing into the storage region are given a “perfect kick” to place them onto a stable orbit. This kick is modeled by applying a 220 Gauss magnetic field throughout the kicker volume for the first revolution. Finally, the storage rate is defined as the fraction of muons surviving 100 revolutions around the storage ring. No muons are allowed to decay in this simulation.

10.6.2 Open-ended vs. Closed-ended Inflector Geometry

The E821 inflector magnet was constructed with a closed end (*i.e.* the superconducting coils wrapped around the end of the magnet) because this greatly reduced magnetic flux leakage into the muon storage region. The impact of the closed end on the horizontal and vertical emittance was studied analytically and with the GEANT tracking software. In the analytic approach, the fraction of muons traversing the inflector ends is studied by comparing the horizontal and vertical beam widths (σ_x, σ_y) after multiple scattering in the material. In this study, a beam filling the horizontal aperture of 18 mm grows to a size of ≈ 35 mm, suggesting that approximately half ($18/35 = 51\%$) of the beam will fail to exit the inflector aperture. With two closed ends the net effect is to lose between 50 – 75% of the incoming beam.

The tracking simulation approach removes the end coils, flange, and window from the GEANT inflector material without altering the magnetic fields. Table 10.9 summarizes the muon storage rates assuming an open and a closed inflector magnet. The beam parameters and inflector aperture are identical in both simulations. Values in parentheses show the results of an incoming beam with a momentum spread of 2% instead of the nominal 0.5%.

Table 10.9: Summary of E821 Inflector Simulations.

Inflector Geometry (Upstream-Downstream)	Muons Generated	Muons Surviving	Storage Fraction
Open-Open	5000 (20000)	664 (691)	13.2±0.3 (3.4±0.1)
Closed-Open	5000 (20000)	522 (593)	10.4±0.3 (2.8±0.1)
Closed-Closed	5000 (20000)	323 (395)	6.5±0.3 (1.9±0.1)
Improvement Factor \equiv Open-Open/Closed-Closed			
	5000 (20000)	-	2.1× (1.7×)
Improvement Factor \equiv Closed-Open/Closed-Closed			
	5000 (20000)	-	1.6× (1.5×)

10.6.3 Sensitivity to Beam Phase-space Matching

A consequence of the limited inflector aperture is gross phase space mismatching into the storage region. This is seen by studying the amplitude of the muon beam (A), which is defined as $A = \sqrt{\beta\varepsilon}$. The maximum horizontal size of a beam clearing the inflector is ± 9 mm, thus, a beam with $\varepsilon = 40$ mm-mrad must have $\beta_x < 2.5$ m and $\beta_y < 19.6$ m. As this beam propagates into the storage region the horizontal β -function subsequently undergoes large oscillations with $\beta^{\max} = 28$ m and $\beta^{\min} = 2.5$ m. This corresponds to a modulation of the horizontal beam amplitude (A) of $r = \sqrt{\frac{\beta^{\max}}{\beta^{\min}}} = 3.4$. This oscillation causes significant beam to be lost on the collimators in the ring.

An alternative to these large oscillations is to perfectly match the β -functions into the storage ring. Assuming a drift space within the inflector ($\vec{B} = 0$), then the β -function at the inflector is defined as $\beta^{\text{inf}} = \beta^{\text{ring}} + s^2/\beta^{\text{ring}}$. The resulting β -functions ($\beta_x^{\text{inf}} = 7.6$ m and $\beta_y^{\text{inf}} = 19.2$ m) requires the incoming beam to be 2.38 times larger than the inflector aperture. Thus, only $1/2.38 = 42\%$ of the beam will clear the inflector. This conclusion follows the GEANT-based tracking result, which shows 53% of the beam clearing the inflector aperture.

10.6.4 Increased Horizontal Aperture

The E821 inflector was constructed with a ± 9 mm horizontal aperture in part due to the double cosine theta magnet geometry and the limited space between the outer main magnet cryostat and the muon storage region. The horizontal aperture also constricts the available phase space in the muon storage region, whose aperture is ± 45 mm.

An augmented inflector “D”-shaped aperture of $\pm 20 \times \pm 28 \text{ mm}^2$ is modeled in the GEANT tracking software. In this study, the main magnet fringe field is assumed to be identically canceled within the inflector beam channel for simplicity. The horizontal beam size is increased allowing for ideal matching to the storage ring β -function, corresponding to $\beta_x = 7.6 \text{ m}$. The horizontal and vertical α Twiss parameters are set to zero in this scenario.

Table 10.10 summarizes the muon storage rates for the two apertures (18 vs 40 mm) and the two end coil inflector geometries (open vs closed) ².

Table 10.10: Summary of E821 Inflector Simulations. The “D”-shaped aperture shown in Fig. 10.6(a) was used. The vertical aperture was 56 mm, the horizontal (radial) aperture was 18 mm, or 40 mm.

Inflector Aperture (Open or Closed ends)	Muons Generated	Muons Surviving	Storage Rate
18 mm Aperture ($A_{\pm 9}$)			
(open ends)	120000	11444	9.5 ± 0.1
(closed ends)	120000	5117	4.2 ± 0.1
40 mm Aperture ($A_{\pm 20}$)			
(open ends)	120000	19161	15.9 ± 0.1
(closed ends)	120000	8706	7.2 ± 0.1
<hr/>			
Improvement Factor $\equiv A_{\pm 20}/A_{\pm 9}$			
(open ends)	-	-	$1.7 \times$
(closed ends)	-	-	$1.7 \times$
Improvement Factor $\equiv A^{\text{Open}}/A^{\text{Closed}}$			
(18 mm Aperture)	-	-	$2.2 \times$
(40 mm Aperture)	-	-	$2.2 \times$
Improvement Factor $\equiv A_{\pm 20}^{\text{Open}}/A_{\pm 9}^{\text{Closed}}$			
	-	-	$3.8 \times$

10.6.5 Summary and Future Simulations

The most recent, but preliminary, simulation that includes

It is clear that we need a full tracking simulation to replace the phase-space models used thus far. The incoming beam to the inflector needs to be optimized for the 18 mm inflector opening, and for 40 mm new inflector. The inflector team will work with the beamline experts to make sure that these essential calculations are high priority.

²Note that these storage rates are computed with a different muon beam and therefore can not be compared directly to the rates in the previous sections.

10.7 ES&H

The superconducting inflector is in a cryostat that includes one section of muon beam tube. The cryostat vacuum is separate from the beam vacuum chamber, so that the inflector can be operated independently of whether the muon beam chamber is evacuated. The cryogenic system, and its operation will follow all Fermilab safety standards for cryogenic and vacuum system operations. This includes, but is not limited to Extreme Cold Hazard, Oxygen Deficiency Hazards. The cryogenics involved are liquid helium and liquid nitrogen. No flammable liquids or gases will be employed. The existing E821 inflector was operated at Brookhaven National Laboratory where similar safety requirements were in place.

10.8 Risks

10.8.1 Relocation Risk

The relocation risk was minimized by careful disassembly and shipping. The E821 inflector is on-site at Fermilab, and as soon as cryogenic capability is available in MC-1, we will set up a test stand in the experimental area outside of the ring to cool and power the inflector.

10.8.2 Other Risks

There is the possibility that some mechanical aspect of the E821 inflector has deteriorated in the 12 years since it was operational, causing the magnet to quench repeatedly before reaching full current. This risk is probably small, since it was tested at KEK, shipped to BNL, installed, and was brought to full current with only a few training quenches. It was very robust in subsequent operation at BNL. The plan to test it as soon as possible at Fermilab will clarify this risk.

At Brookhaven a helium leak in the valve box or lead-pot developed. After examining the situation after transport, it has been decided to re-build this part of the inflector system, rather than repair the existing one. There is a small risk that the leak was in the magnet itself, but this is viewed as extremely unlikely by Akira Yamamoto, who supervised the engineering design and construction, and Wuzheng Meng, who did the magnetic design and was responsible for its operation at BNL.

The most sensitive part of the re-installation is reconnecting the inflector leads. Our technician Kelly Hardin was involved in the disassembly at BNL, and understands the issues involved in the reconnection very well.

10.9 Quality Assurance

Proper quality assurance is essential in the transport and reassembly of the inflector magnet. The mechanical aspects, heat shield, etc. will be carefully examined for issues, once the inflector arrive at Fermilab. It will be determined as quickly as possible whether the inflector meets the Muon g-2 requirements for performance and reliable operation. Quality Assurance

will be integrated into all phases of the transport and reassembly work. including design, procurement, fabrication, and installation.

10.10 Value Engineering

The baseline is to begin the experiment by re-using the existing E821 Inflector. A new inflector with a much larger horizontal aperture could permit two to three times as many muons to be stored. A gain of this factor would significantly improve the statistical reach of the experiment, and permit more beam time to be used for systematic studies.

Thus a new inflector would present a significant opportunity to improve the experiment and to use running time more effectively. At present there is insufficient funding in the project to develop and produce a new inflector. Nevertheless, given the potential benefit, we will continue to support the preliminary design of a new inflector, in order to understand the cost of such a device. Should sufficient contingency be earned back from other areas of the project, we will proceed with final design and implementation.

References

- [1] The Inflector Task Force: Lee Roberts (Chair - Boston); Bill Morse, Brett Parker, Vladimir Tishchenko (Brookhaven); David Rubin (Cornell), Emanuela Barzi, Thomas Gadfort, Carol Johnstone, Vladimir Kashikhin Jim Morgan, Hogan Nguyen, Chris Polly, Alexander Zlobin (Fermilab); David Kawall (U. Mass.); David Hertzog, Nathan Froemming (Washington).
- [2] A. Yamamoto, et al., Nucl. Inst. Meth. **A 491**, 23 (2002).
- [3] Many of the details are given in Wuzheng Meng, Non-Ferrous Superconducting Magnets, Ph.D. Dissertation, Boston University, 1991.
- [4] Frank Krienen, Dinesh Loomba and Wuzheng Meng, Nucl. Inst. Meth. **A238**, 5 (1989).
- [5] A. Yamamoto, Nucl. Instr. and Meth. A 453 (2000) 445.
- [6] Y. Makida, et al., IEEE Trans. Magn. 27(2) (1991) 1944.
- [7] M. Garber, A. Ghosh, W. Samson, IEEE Trans. Magn. 25 (2) (1989) 1940.
- [8] Y. Saito, et al., Development of beam inflection superconducting magnet evaluation of prototype, Tokin Technical Review, No. 20.
- [9] M.N. Wilson, Superconducting Magnets, Oxford Science Publications, Oxford, 1983.
- [10] A. Yamamoto, Status of the inflector, Internal Meeting Minutes, 1992; W. Meng, K. Woodle, Superconducting shield test on ($g - 2$) inflector magnet, ($g - 2$) Note, No. 210, 1994.
- [11] M.A. Green, W. Meng, IEEE Trans. Appl. Supercond. 5 (2) (1995) 667.
- [12] G.T. Danby, W. Meng, W. Sampson, K. Woodle, IEEE Trans. Magn. 30 (4) (1994) 1766.
- [13] I. Itoh, T. Sasaki, IEEE Trans. Appl. Supercond. 3 (1993) 177.
- [14] H.N. Brown, et al, Phys. Rev. Lett. **86** 2227 (2001).
- [15] F. Krienen, et al., IEEE Trans. Appl. Supercond. **5** (2) (1995) 671.
- [16] W. Meng, K. Woodle, Superconducting shield test on g-2 inflector prototype, g-2 Note, No. 210, 1994.

- [17] The $g - 2$ Collaboration: G.W. Bennett et al., Phys. Rev. Lett. **89**, 101804 (2002); Erratum-ibid. **89**, 129903 (2002).
- [18] Bennett GW, et al. (The $g - 2$ Collab.) Phys. Rev. Lett. 92:161802 (2004)
- [19] Rick Hance, Dzero Solenoid Quench Protection and Operation, <http://www-d0.fnal.gov/hance/solenoid.htm>
- [20] Walter Jaskierny, "G-2 Inflector Voltage Tap Illustration", PDF Drawing, docdb documents, docdb# 1915-v1.
- [21] <http://www.bnl.gov/magnets/Staff/Parker/>
- [22] Brett Parker, private communication, March 2013.
- [23] Lance Cooley, Fermilab. Private Communication.
- [24] Steve Smith at MTI Metal Technology. <http://www.mtialbany.com/>
- [25] Tony Nelson at ATI Wah Chang. <http://www.atimetals.com/>
- [26] See e.g. B. Parker and J. Escallier, "Serpentine Coil Topology for BNL Direct Wind Superconducting Magnets," PAC05, Knoxville, Tennessee, May 16-20, 2009 p. 737-739; W. Bertsche et al., A magnetic trap for antihydrogen confinement, Nuclear Instruments and Methods in Physics Research, vol. A566, pp. 746756, 2006.
- [27] B. Parker, et.al., "Direct wind superconducting corrector magnets for the SuperKEKB IR," International Particle Accelerator Conference IPAC'12, New Orleans, USA, May 20 - 25, 2012. B. Parker, et. al., "Superconducting corrector IR magnet production for SuperKEKB," 25th North American Particle Accelerator Conference, NA-PAC'13, Pasadena, California, USA, September, 2013.

